DEVELOPING AN APPROACH TO IMPROVE BETA-PHASE PROPERTIES IN FERROELECTRIC PVDF-HFP THIN FILMS

A Thesis

Submitted to the Faculty

of

Purdue University

by

Ashley S. Dale

In Partial Fulfillment of the

Requirements for the Degree

of

Master of Science

May 2020

Purdue University

Indianapolis, Indiana

THE PURDUE UNIVERSITY GRADUATE SCHOOL
STATEMENT OF THESIS APPROVAL

Dr. Ruihua Cheng, Chair

Department of Physics

Dr. Horia Petrache

Department of Physics

Dr. Stephen Wassall

Department of Physics

Approved by:

Dr. Ricardo Decca

Head of the Department of Physics Graduate Program

ACKNOWLEDGMENTS

I would like to express my deep gratitude to Dr. Ruihua Cheng for her mentorship and for the opportunity to contribute to her research group and laboratory. Dr. Cheng, thank you for giving me a "Physics Home."

My work and studies would not have been possible without the continued financial support and mentorship of Dr. Lauren Christopher and the IUPUI Electrical Engineering Department. Dr. Christopher, thank you for encouraging me to pursue my passions and giving me the resources to do so; I am beyond grateful to you.

I also would like to express thanks to Aaron Mosey for his ongoing technical and scientific support, machine shop training and sanity-preserving friendship. Words fail to adequately describe his contribution to this thesis.

A significant portion of this project would not have occurred without the thoughtful conservatorship of Dr. Bruce Ray, who produced the original KSV equipment that pushed this thesis in a new direction entirely.

Many thanks are due to Dr. David Emerson for his lessons in reverse engineering hardware and writing code. A good portion of this project would have failed without Dave's generous donation of time and knowledge regarding COM ports.

I also would like to thank my comittee members Dr. Horia Petrache and Dr. Stephen Wassall for their insights and support during this process.

Shout-outs to my group members Saeed Yazdani, Joseph Soruco and Jared Phillips, and friends Thomas Bsaibes, Muchuan Hua, Kaustubh Agarwahl and Azam Shafieenezhad for their help and camaraderie.

Further recognition goes to administrative staff Sherrie Tucker, Juli Craft, Clair Schaler, and Kathie Riley. Thank you for always having my back.

Finally, I need to acknowledge the constant love, support and encouragement of my grandparents, parents, and sisters. Sarah, thank you for being my reader and

photo-editor. Grace, thank you for sharing your extremely nice camera. Faith, you are my favoritest lab assistant ever. My love to you all.

TABLE OF CONTENTS

LIST OF FIGURES

Figure Page

Figure Page

ABBREVIATIONS

AFM	Atomic Force Microscopy
DSC	Differential Scanning Calorimetry
FE	ferroelectric, ferroelectricity
FTIR	Fourier Transform Infrared Spectroscopy
LB	Langmuir-Blodgett
ML	monolayer
PVDF	polyvinylidenefluoride
PVDF-HFP	polyvinylidenefluoride-hexafluoropropylene
PVDF-TrFE	polyvinylidenefluoride-trifluoroethylene
SEM	Scanning Electron Microscopy
XRD	X-ray Diffraction

ABSTRACT

Dale, Ashley S. M.S., Purdue University, May 2020. Developing an Approach to Improve Beta-phase Properties in Ferroelectric PVDF-HFP Thin Films. Major Professor: Ruihua Cheng.

Improved fabrication of poly(vinylindene fluoride)-hexafluoropropylene (PVDF-HFP) thin films is of particular interest due to the high electric coercivity found in the β-phase structure of the thin film. We show that it is possible to obtain high-quality, β-phase dominant PVDF-HFP thin films using a direct approach to Langmuir-Blodgett deposition without the use of annealing or additives. To improve sample quality, an automated Langmuir-Blodgett thin film deposition system was developed; a custom dipping trough was fabricated, a sample dipping mechanism was designed and constructed, and the system was automated using custom LabVIEW software. Samples were fabricated in the form of ferroelectric capacitors on substrates of glass and silicon, and implement a unique step design with a bottom electrode of copper with an aluminum wetting layer and a top electrode of gold with an aluminum wetting layer. Samples were then characterized using a custom ferroelectric measurement program implemented in LabVIEW with a Keithley picoammeter/voltage supply to confirm electric coercivity properties. Further characterization using scanning electron microscopy and atomic force microscopy confirmed the improvement in thin film fabrication over previous methods.

1. INTRODUCTION

As long as the need for faster, cheaper, and more environmentally friendly technologies exists, there will be a coexisting need to develop materials and fabrication methods to support these new technologies. The choice to develop organic polymers as a viable solution to technical challenges is partly motivated by the historical successes of one polymer in particular: poly(vinylidene fluoride) (PVDF).

First synthesized in 1944 by Dupont and brought to market in 1961 by Pennsalt [1], PVDF has been extensively analyzed in the fields of physics, chemistry, and materials science. There are many industrial applications for PVDF in its amorphous form, including wire coatings, insulation and additives to teflon. [2]. In its crystaline form, existing applications for PVDF include transistors [3, 4], sensors (e.g. pressure, heat, nerve gas) [3, 5–9], molecular electronics [3, 10], portable electronic devices [5, 9], energy harvesting systems/transducers [4, 5, 7–9, 11], water purifying devices [5], gas separation [5], super-hydrophobic materials [4], and solar cells [4].

In these devices, the ferroelectric, pyroelectric, and piezoelectric properties of PVDF may be accessed directly or in conjunction with other material properties to create sophisticated behaviors. For example, in the design and fabrication of molecular electronics, new applications have been discovered for PVDF and its copolymers. By combining spintronics with advances in molecular electronics, nonvolatile voltage control of molecular spin state has been achieved at room temperature in a spintronic device that opens the door to a new class of transistor technology [10]. The device structure utilizes the proximity effect of a spin-crossover (SCO) molecule layered with a ferroelectric β-phase PVDF-HFP thin film [10]. Polarizing the PVDF-HFP in its β-phase creates an external electric field that can be used to switch the spin state of the SCO molecule due to magneto-electric coupling as shown in Figure 1.1 [10]. The PVDF-HFP polarization is persistent and controllable through an externally

applied voltage, resulting in a nonvolatile, voltage controlled spintronic device with bistability [10].

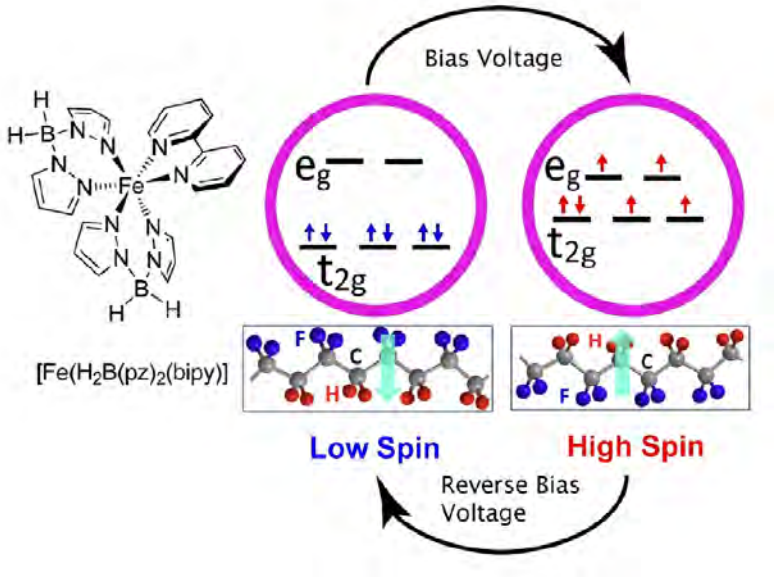

Figure 1.1. The spin cross over molecule $Fe(H_2B(pz)_2)_2(bipy)$ may be manipulated between the high spin and low spin states by applying the external coercive electric field of the PVDF generated from the dipole moment of the PVDF molecule as shown by Hao et al. [10]. Figure from [10].

All of these applications implement unique properties of PVDF in its various forms to achieve desirable outcomes, but the implications of organic, room temperature molecular transistors are staggering. The functionality of the molecular electronic device previously described relies on the quality and reliability of the ferroelectric polymer coupled with the SCO, specifically on the capability of the ferroelectric thin film to maintain polarization and to switch polarization without fatigue. A clear approach must be established for controlling the parameters which imbue the ferroelectric polymer with its desirable characteristics while minimizing unwanted behaviors. According to work by Tagantsev et al., ferroelectric performance in general decays due

to microscopic issues with electron injection and oxygen vacancies. and addressing these problems successfully requires a material-centric approach [12].

To optimize device design, further improvement is sought in the number of switching cycles the device can sustain and in the magnitude of the device's electric coercivity. Hao et al. report a device capable of switching polarity twice [10]; however the ability of other ferroelectrics to switch upwards of 10^{12} times [12] hints at greater capabilities. Hao et al. reported coercive field of ∼100 MV for their PVDF-HFP thin film [10], but this characteristic is largely determined by the percentage of the β-phase in the thin film [13]. A high coercive field is desirable, as this property helps prevent relaxation or accidental switching of the SCO state.

The immediate challenges of ferroelectric fatigue and obtaining a high electric coercive field in PVDF-based molecular electronics are outgrowths of the challenges found in fabricating high-quality ferroelectric PVDF-HFP thin films. Accordingly, a brief discussion of the physical model for ferroelectricity in Section 1.1 provides the necessary context for understanding the ferroelectric measurement methods presented in Section 3.1. An analysis of the properties of organic ferroelectric polymers in general, and PVDF-HFP in particular is presented in Section 1.2 to create motivation for the development of an automated deposition system in Section 2.2.1. The intent of this thesis in its entirety is to provide a clear path towards improved ferroelectric behavior in PVDF-HFP by placing proven experimental techniques in the context of optimizing the β-phase percentage in the crystal.

1.1 Ferroelectricity

The well-established date for the discovery of the class of materials containing ferroelectric behavior is 1824, when Brewster termed pyroelectricity to describe electrical polarization arising from self-ordering properties induced by a change in temperature in Rochelle Salt ($NaKC_4H_4O_6{\cdot}4H_2O$) [14]. Despite this auspicious start, progress towards developing a working knowledge of ferroelectricity was slow in coming–the next

major accomplishment in ferroelectrics was achieved by the brothers Curie in 1880. Together, the Curies discovered–and accomplished a systematic study of–piezoelectric properties in Rochelle Salt, quartz, and other crystals, going to great lengths to describe the electrical polarization arising from self-ordering properties induced by mechanical stress [14–16]. The work by the Curies is particularly relevant in that it explicitly connects piezoelectric behavior to crystal structure [15]. In 1894, Friedrich Pockels–brother to Agnes Pockels, inventor of the trough apparatus now used to create ferroelectric thin films–identified anomalous dielectric behavior in Rochelle Salt, and this work provided a popular approach to identifying other possible candidates for ferroelectricity [17].

By the beginning of the 20th century, pyroelectricity, piezoelectricity and dielectric behavior had laid the ground work for the discovery of ferroelectricity in 1921 by Valasek [18]. Ferroelectricity (FE) derives its name, and therefore inherits some connotations, from ferromagnetism [18]. Just as ferromagnetism describes the material property of spontaneous magnetization, the name ferroelectricity hints at the ability of a material to maintain a persistent electric polarization in the absence of an external electric field. Specifically, a ferroelectric material under an applied electric field produces an electrical-polarization hysteresis loop analogous to the magnetization hysteresis loop produced by a ferromagnetic material under an equivalent magnetic field: the electrical polarization must be bi-stable and reversible [11]. Ferroelectricity is an intrinsic property of certain noncentrosymmetric crystals such that ferroelectric, pyroelectric and piezoelectric behaviors are intrinsic to the 10-point crystal structure of all ferroelectrics [11].

The underlying physical mechanisms for ferroelectric behavior continue to be deeply investigated, sometimes contentiously so [19, 20]. Ferroelectric behavior arises from aligning the dipole moments of small domains encompassing a quantity of electric charge (referred to as *electrets*) within a crystal; the bulk behavior of the electrets results in the polarization observed in a crystal [21].

Electrets may align under an applied electric potential with varying types of cooperativity [21]. Cooperativity that favors parallel alignment between permanently-dipole electrets and allows the system to be in equilibrium results in ferroelectricity, while minimal cooperativity may result in a temporary polarization that ultimately relaxes to a non-polarized equilibrium state due to trapped space charges [21].

This definition of ferroelectric behavior precludes any type of amorphous material, and many crystalline materials, from being considered ferroelectric. Ferroelectricity is attributed to the permanent dipole moment throughout the crystal alone; any contributions to ferroelectric behavior from space charge accumulation and charge injection must be discounted.

Two ferroelectric switching mechanisms for electrets have been identified: intrinsic and extrinsic. During extrinsic switching, polarization domains overcome their walls to merge during an experimentally observed growth process [22–24]. Intrinsic, or homogenous, switching occurs when "an electric field is large enough to overcome the energy barrier associated with the long-range correlation of the polarization" [25] resulting in the simultaneous polarization of all dipoles in a single domain [25, 26].

This switching process is frequently represented by an electric hysteresis curve, such as the hysteresis curve for a ceramic ferroelectric capacitor shown in Figure 1.2. In Figure 1.2, the x-axis intercepts depict the electric coercivity of the sample, and the y-axis intercepts depict the remanent polarization. The maximum and minimum y-values on the hysteresis curve represent the positive and negative saturation of the sample. It is worth noting that any time a reported remanent polarization is greater than the net dipole moment of a material, ferroelectricity is not the sole contributor to the polarization [21].

As we approach the 200th anniversary of the discovery of pyroelectricity in Rochelle Salt, a large class of ferroelectric ceramics has been discovered, including lead zirconate titatnate (PZT), lead lanthanmum zirconate titanate (PLZT), lead magnesium niobate (PMN), lead titanate (PT), lead zinc niobate (PZN), lead stannate zirconate titanate (PSZT), lead zirconate (PZ), barium strontium titanate (BST), barium ti-

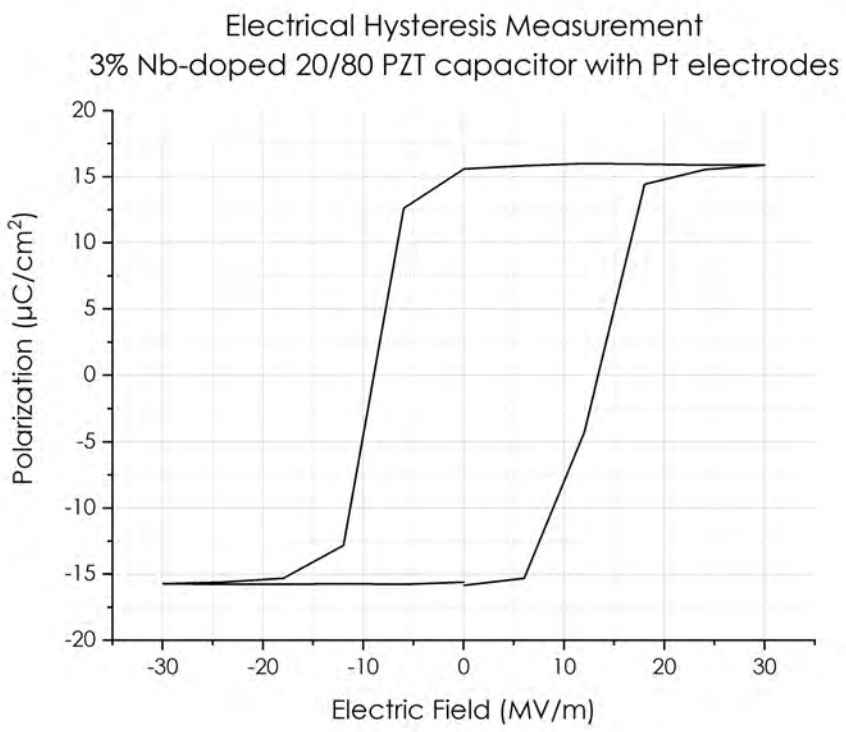

Figure 1.2. Electric Hysteresis Loop for a ferroelectric capacitor. The electrical response of the capacitor is measured while an applied electric field is varied from zero to maximum, maximum to minimum, and from minimum to zero.

tanate ($BaTiO_3$) and strontium bismuth titanate (SBT) [14]. In 2018, ferroelectric behavior was confirmed at the nanoscale in $Hf_{0.5}Zr_{0.5}O_2$ thin films [27]. However, the class of ferroelectric polymers remains quite small as discussed in Section 1.2.

1.2 Organic Ferroelectric Polymer Vinylidenefluoride with Copolymer Hexafluoropropylene

The desired characteristics of a FE polymer thin film are dictated by the application. Specifically, an attractive FE polymer thin film may have qualities such as established fabrication and manufacturing methods, mechanical properties such

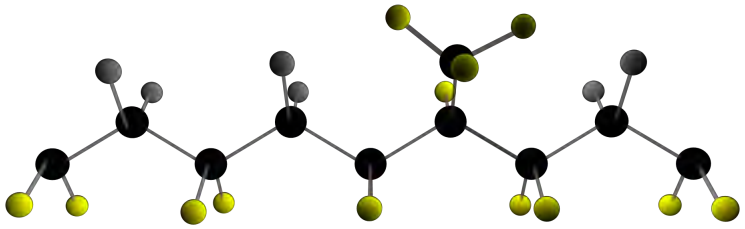

Figure 1.3. The PVDF-HFP molecule structure in the β-phase orientation consists of two repeating blocks $(\text{-}CH_2CF_2\text{-})_x[\text{-}CF_2CF(CF_3)\text{-}]_y$. Alternating pairs of H (shown in gray) and F (shown in yellow) follow the C (shown in black) backbone except in the case where a single F is replaced by the copolymer HFP containing an additional C and three more Fs.

as flexibility, toughness and conformability, electric properties such as high coercivity and electro-mechanical coupling, and optical properties such as translucence and nonlinearity. [3, 5, 8, 11, 28].

Poly(vinylindene fluoride) (PVDF) has a repeating structure of (CH_2-CF_2), and was the first molecule discovered to belong to the exclusive class of ferroelectric (FE) polymers [29]. Although other potential class members have been fabricated, many lack the same strong FE characteristics demonstrated by PVDF and/or there is uncertainty regarding what mechanism gives rise to the supposed FE behavior [21, 30]. For example Poulsen et al. discuss replacing the fluorines on in PVDF with chlorines to create the poly(vinylidene chloride) (PVDC) molecule which is identical in structure to PVDF but with very different properties: the dipole moment of the molecule is reduced due to the lower electronegativity of chlorine, and the increased covalent radius of the chlorine atoms compared to the fluorine atoms inhibits the formation of a crystal structure that can support ferroelectricity [21].

Five crystal phases have been experimentally observed in PVDF; these are synonymously named according to order of discovery and phase. The α-phase (phase II) represents the polar $TGT\bar{G}$ conformation, the β-phase (phase I) represents the polar $TTTT$ conformation, the γ-phase (phase III) represents the polar $TTTGTTT\bar{G}$ formation, and the δ-phase (phase IV or polar form II) is the non-polar version of the α-phase [31]. Discovered transitions between these phases are shown in Figure 1.4 as summarized from references [9,31,32]. The ε-phase (phase V) is the non-polar version of γ-phase. An additional sixth phase, ζ-phase, has been predicted as the non-polar form of the β-phase but is not yet experimentally confirmed [33].

Of the five experimentally observed phases, the β-phase possesses the highest dipole moment and the strongest piezoelectric, ferroelectric, and pyroelectric properties [9]. This is largely due to the additive dipole moment found in the all-trans configuration [9]. As shown in Figure 1.4, there are multiple methods for directly obtaining β-phase crystal structure, including Langmuir-Blodgett deposition, spin coating, electrospinning, solvent casting in general and specifically from hexamethylphosphoramide (HMPTA), epitaxial growth, and high-pressure quenching. [9,13,31,32,34–39]. Langmuir-Blodgett deposition is discussed at length in Section 2.2.1.

In addition to the methods in Figure 1.4, PVDF may be paired with copolymers trifluoroethylene (TrFE) [7, 8, 40–42] or hexafluoropropylene (HFP) [5, 38, 39, 42, 43] to encourage β-phase formation. A representation of PVDF with its HFP copolymer is shown in Figure 1.3. These copolymers act to repel other molecular chains, aiding in self-ordering and encouraging crystal formation. However, the inclusion of a copolymer has a significant effect on the dipole moment–and by extension the FE properties–of the crystal. For example, the remanent polarization of PVDF-HFP depends on the percentage of the copolymer present, where 5 mol% decreases the remanent polarization to zero [42]. While PVDF has an electrical dipole moment of 5-8x10^{-30}C·m [32], the dipole moment of PVDF-HFP is less due to the decreased moment between the C-C bond. Finally, analysis of X-ray diffraction data shows

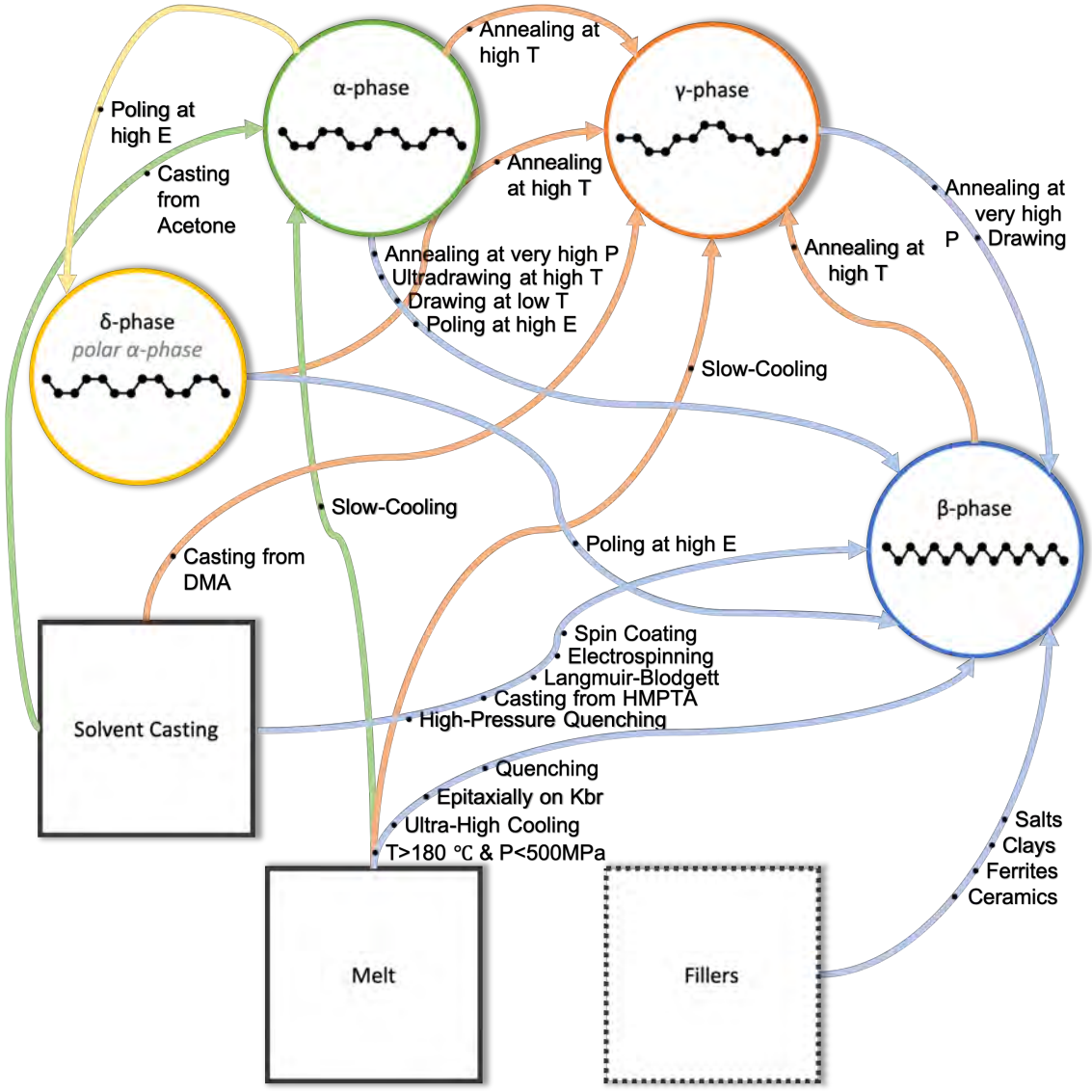

Figure 1.4. Overview of processes which culminate in β-phase PVDF crystal structure. Crystal phases are denoted in circles with a depiction of the relevant configuration, physical processes used as a starting point for obtaining crystalline structure are denoted in squares. Compiled from [9, 31, 32].

that the ratio of HFP copolymer to PVDF has a definitive impact on crystal lattice spacing [39].

The result is a balancing act between the practicalities of thin film formation and manipulation, and maintaining the thin film properties that inspired these efforts.

2. THIN FILM FABRICATION

Ferroelectric (FE) PVDF thin films are not only desirable, but also achievable through a variety of methods as shown in Figure 1.4. In fact the sheer number of methods hinted that additional methods may exist, and work by Carvell confirmed it: FE PVDF thin films may be fabricated by simply hand-dipping a substrate in a PVDF thin film created in a beaker of water–perhaps the ultimate reduction in complexity for thin film fabrication [3].

However, attempting to apply Carvell's thin film fabrication techniques quickly exposes the the lack of quality control inherent to this approach. Further review showed that inconsistent quality is not unique to Carvell; variability in PVDF thin film fabrication is reported throughout literature. For example, one source reports a monolayer with thickness of approximately 0.5 nm [19] while another source reports nearly four times the thickness [8].

This research is focused on identifying the most relevant parameters to FE PVDF thin film fabrication, with an experimental approach focused on two goals: First, to build a system that improves on past methods used by our laboratory for creating LB thin films. Second, to quantify this improvement through repeatable characterization techniques.

In Section 2.2, the first goal of improving past methods for LB thin films is accomplished through the development of an automated LB deposition system. The development process and design decisions for hardware and software controls over the sample fabrication process are discussed. Specific parameter values in the sample fabrication process are provided.

In Chapter 3, the second goal, quantifying the success of the system from section 2.2, is accomplished. Sample characterization data is shown and discussed.

Comparison data for samples discussed in section 2.1 and samples fabricated without the automated system is analyzed when available.

2.1 Sample Design and Fabrication

2.1.1 Overview

Samples are fabricated on silicon and glass substrates using a multi-step, multi-method deposition process. An overview of the deposition process is presented here, with details of methods presented in subsequent sections.

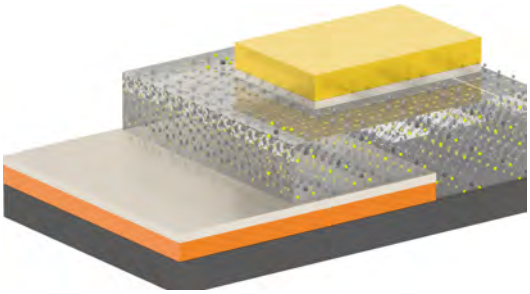

Figure 2.1. Example Sample Structure. From bottom to top: substrate, Cu layer, Al_2O_3, PVDF-HFP, Al_2O_3, Au layer.

Glass and silicon substrates are excellent choices as for this study. The uniform crystal nature of a Si wafer facilitates the collection of low-noise X-ray diffraction (XRD) data, while the polished surface creates a uniform surface for potential nucleation sites with new Si wafers encouraging α-phase structure and reused Si wafers encouraging γ-phase structure [44]. Glass laboratory slides are abundant and inexpensive while the insulating properties of glass are useful during electrical measurements. Both glass and silicon are hydrophilic when thoroughly cleaned [45]; this property is important due to the H_2O subphase used later in the fabrication process.

The substrate is sonicated for 30 minutes in a solution of DI water and Alconox. After sonication, the substrate is rinsed in DI water, then sequentially submerged for

five minutes each into warm baths of acetone, methanol and isopropanol heated to approximately 50 °C. After the solvent baths, the substrate is rinsed in 18 MΩ MilliQ H_2O and dried.

After cleaning, a temporary mask of aluminum foil is applied to the substrate and a bottom electrode is deposited onto the substrate surface using magnetron sputtering deposition and thermal evaporation. The details of these processes are discussed in Sections 2.1.2 and 2.1.2 respectively. The Al foil mask prevents the electrode from covering the entire substrate surface during the deposition process, aiding in the creation of smaller, more uniform samples. Additionally, the mask permits deposition of a separate dummy-electrode by allowing limited deposition outside of the main sample area in the substrate's upper corner. This dummy-electrode allows for determination of the final bottom electrode thickness by atomic force microscopy (AFM) after the sample fabrication process is completed.

Samples with successful ferroelectric characterization implement a 3nm wetting layer of Al_2O_3 above and below the PVDF-HFP thin film; this structure is shown in Figure 2.1. The addition of an Al_2O_3 wetting layer is multi-purpose: the use of oxide electrodes has been shown to help reduce sample fatigue during ferroelectric measurements [16, 46, 47], Al_2O_3 is hydrophilic and maintains the hydrophilicity of the insulating substrate [48], and, since Al_2O_3 is insulating [49], the additional layers of insulation help prevent the ferroelectric capacitor from electrically shorting should the polymer thin film deposit unevenly.

The mask used to create the bottom electrode is then removed, and the sample may be cleaned in the solvent baths a second time to remove any dust or contamination that occur during handling. Sonication with the Alconox solution is omitted, as it may disturb the bottom electrode metallic thin film.

Next, a poly(vinylindene fluoride)-hexafluoropropylene (PVDF-HFP) thin film is deposited on the substrate and bottom electrode using an automated Langmuir-Blodgett (LB) method. The LB deposition is such that the PVDF-HFP thin film

overlaps both the bare substrate and the sputtered electrode. This overlap is shown in Figure 2.1. Details of the LB deposition are presented in Section 2.2.3.

Finally, a second Al foil mask is applied to the sample and a top electrode is thermally evaporated onto the sample. The Al foil mask for the top electrode is designed to allow multiple small capacitors to share the bottom electrode on a single sample. This allows for repeated measurement of the same thin film should part of the sample be destroyed during the characterization process. The top electrode overlaps only partially with the bottom electrode, helping to preserve the sample during electrical measurements by reducing the size of the electrode area [12]. Furthermore, the top electrode does not extend to the edge of the polymer thin film, helping to prevent edge effects during electrical measurements. Samples with successful ferroelectric characterization featured a top electrode with 3 nm layer of Al_2O_3 capped by 100 nm of Au.

The insulating substrate, bottom electrode, polymer thin film, and top electrode form a ferroelectric capacitor, as shown in Figure 2.1.

Figure 2.2. Sample fabricated using magnetron sputtering, automated LB deposition, and thermal evaporation. Five 3 mm^2 capacitors are situated along the upper left edge. Two characterization electrodes are visible on the lower right edge. Silver paint for connecting the capacitors to gold wire is visible on the bottom electrode and third top electrode.

A completed sample is shown in Figure 2.2 with five ferroelectric capacitors sharing a single bottom electrode. The substrate area in Figure 2.2 is 2.5 cm^2, and each capacitor is 3 mm^2. In Figure 2.2, the silver paint used during electrical measurements is visible on the center top electrode pad and on the bottom electrode. Two calibration electrodes on the upper edge are clearly visible and not electrically connected to the five capacitors on the same substrate.

After fabrication, the sample is ready to be characterized.

2.1.2 Physical Vapor Deposition

Magnetron Sputtering

Sputtering is the process of removing atoms from a target surface by bombarding the target with ions generated in a plasma, then allowing the freed atoms to condense on a substrate positioned above the target [51]. It is a highly energetic process; the plasma contains electrons freed from the target surface in addition to the electrons native to the plasma [51]. Work by Stuart and Wehner places the average energy of sputtered Cu atoms in the range of 2.6 eV to 15 eV [52], and the average energy sputtered energy of Au atoms at 9 eV–more than 100 times the energy of thermally evaporated Au atoms [53]. As a result, thin films form very quickly across the substrate; this makes sputtering an excellent method for depositing the bottom electrode.

The addition of a magnetic field applied parallel to the target surface during sputtering helps to direct the secondary electrons towards the substrate by causing the electrons on the target surface to move in a closed, circular path that creates a vortex-like plasma beam [54]. This applied magnetic field may take two forms, known as balanced and unbalanced magnetron sputtering. During balanced magnetron sputtering, the plasma beam formed by the magnetic field traps some ions near the target surface [54]. These trapped charges inhibit sputtering, causing uneven deposition across the substrate surface. The trapping effect of the applied magnetic field is mit-

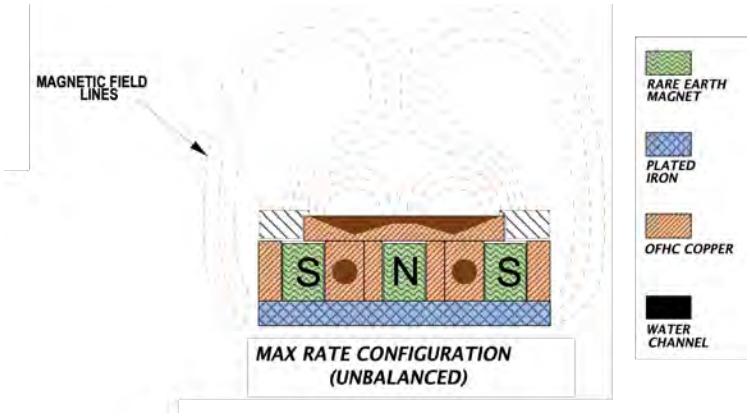

(a) Unbalanced magnetron sputtering configuration in the AJA A320 sputtering source with the magnet orientations shown. Modified from AJA Installtion Manual [50].

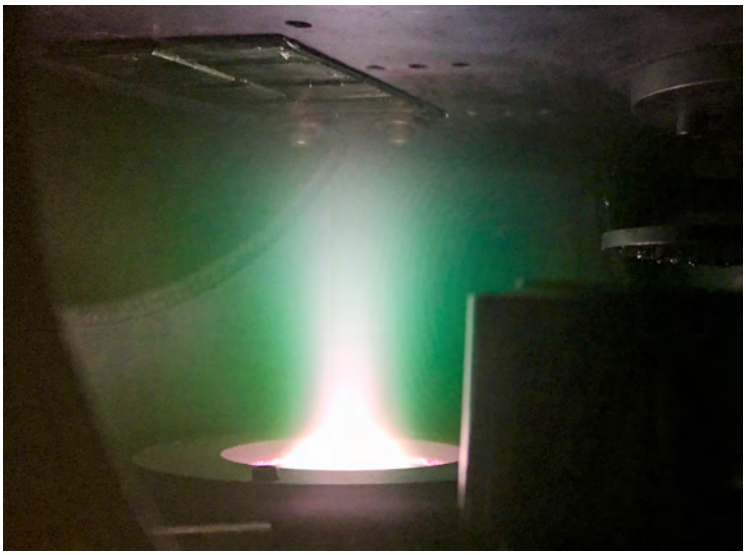

(b) Magnetron sputtering Cu onto glass substrate covered in Al foil masks. The discharge plasma is clearly visible, and has a bright green glow along the outer edges, and a violet glow beneath the cathode ring (barely visible in this image at the base of the plasma beam).

Figure 2.3. Unbalanced magnetron sputtering deposition of bottom electrodes on sample.

igated in unbalanced magnetron sputtering by relaxing the field just enough for the trapped species to escape as shown in Figure 2.3(a) [55]. This allows for the plasma to become more reactive, and results in more uniform coverage of the substrate.

For this project, an on-axis DC unbalanced magnetron sputtering system with an AJA A320 magnetron sputtering source was used to deposit 120 nm of Cu onto the substrates. An Ar environment at 10 mTorr pressure provided the source for the plasma, and deposition occurred at a rate of 2.2 Å/sec with 30 Watts power applied to the gun. Magnetron sputtering is an excellent choice due to the even coverage of the substrate and the quick deposition rate. The deposition of the bottom electrodes onto glass slides with Al foil masks is shown in Figure 2.3(b).

Thermal Evaporation

Before use in thermal evaporation, the tungsten-alumina wire baskets used for evaporation were calibrated under vacuum with a chromel-alumel (K-type) thermocouple to establish a correlation between applied current and basket surface temperature. Calibration data for the tungsten-alumina baskets may be found in Appendix section B.1.

Thermal evaporation is used three times during sample fabrication: for the bottom Al_2O_3 layer, the top Al_2O_3 layer, and the top Au electrode.

The bottom Al_2O_3 layer utilizes thermal evaporation (as opposed to sputtering) due to the need for an extremely uniform thin film with minimal thickness. The Al_2O_3 thin film evens out the roughness inherent to magnetron sputtering deposition. The lower energy and deposition rate of thermal evaporation allows for better control of the deposition process and helps to ensure that these requirements are met.

Thermal evaporation for the top electrode is required because it is gentle enough to preserve the soft polymer crystal structure already on the sample. The high energy of magnetron sputtering would likely cause the polymer to collapse.

Figure 2.4. Calibrating empty tungsten alumina crucible with K-type thermocouple. In the bottom right corner of the image, the crucible for aluminum is on the left and the crucible for gold is on the right.

To begin the deposition process, a tungsten-alumina wire basket is filled with 99.999% Al shot or 99.995% Au wire as required. The basket is located inside the sputtering chamber under vacuum, and is connected to an external current supply via a high-current feed through. The basket is brought to the deposition temperature over a period of 20 minutes by gradually increasing the current.

A 3 nm layer of Al_2O_3 is deposited at ~930K under vacuum with a pressure of $\sim 10^{-6}$ Torr for both the top and bottom electrodes. This Al thin film is then exposed to atmosphere for 24 hours to allow a thin layer of Al_2O_3 to form.

For the top electrode, after the Al_2O_3 has formed a 100nm layer of Au is evaporated onto the sample at ∼1300K under vacuum with a pressure of $\sim 10^{-6}$ Torr.

The temperatures for thermally evaporating the Al and Au thin films were purposefully chosen to be below the respective boiling points for these metals. This helps ease the evaporation process, ensuring that the film does not grow too quickly and damage the polymer thin film or entirely cover the Cu bottom electrode.

2.2 Developing an Automated Langmuir Blodgett Deposition System

2.2.1 Langmuir Blodgett Thin Film Deposition

Langmuir-Blodgett (LB) thin film deposition refers to a method by which a preformed thin film on the surface of a liquid subphase is cast onto a solid substrate. LB deposition methods are well suited for use with amphilic molecules, as these molecules self-orient on the subphase surface according to the dipole moment of the molecule. This self-orientation is maintained when the thin film is transferred to the substrate through the dipping process, allowing for macroscopically controlled molecular assemblies.

The use of a trough with barriers to maintain surface tension and manipulate a thin film on a liquid subphase was pioneered by Pockels [56], with the design later modified by Langmuir [57] and others. While Pockels' trough was made of tin, Fox and Zisman used PTFE [45] and this material continues to be a popular choice, though not the only choice.

Thin film troughs are modifiable depending on experimental configuration and purpose. When used during studies of surface tension, the trough may be accessorized as Pockels' was with a surface balance and various microscopy tools for the observation and control of surface dynamics. When used as part of the LB deposition process, a trough accessorized with a reservoir for dipping and a sample dipping mechanism enables increased control over deposition parameters, leading to more uniform thin

film samples. Temperature control of the subphase and pressurized environments of noble gasses are also common additions to the trough experimental setup.

The barrier arms on the LB trough help maintain a constant thin film to surface area ratio. Thin film is removed from the subphase surface as it is transferred on to the substrate; the barrier arms compress the surface area to compensate for the removed thin film.

The vertical dipping method of creating multi-layer thin films through monolayer (ML) deposition was developed by Blodgett and Langmuir [58]. In their 1937 paper, Blodget and Langmuir use the deposition of Barium Stearate on a substrate of glass or metal to expound on several key issues in the deposition process: deposition of the first layer, the speed at which the substrate may be removed from the subphase, and interference caused by debris in thin film formation [58]. These issues continue to be well documented throughout literature; while debris may be prevented from contaminating a film through careful environmental control (i.e. proper cleaning and care of equipment; processing thin films in a hood, glove box or clean room), the deposition of the first layer and the role of speed in the deposition process continue to be explored [4, 59].

The physical transfer of thin film from subphase surface to substrate surface occurs at the meniscus formed by the three phases present in the experiment: the solid substrate, the liquid subphase, and the gaseous environment in the laboratory. This paradigm is shown in Figure 2.5. Not only do the meniscus area and contact angle directly affect the transfer of thin film to substrate, the formation of solids in the meniscus phase as shown by Riegler and LeGrange [60, 61] may increase the quantity of material transferred beyond a single ML [45]. As a result, control of the contact angle between subphase and substrate is of great value when fabricating thin film samples.

Several models exist relating the role of the dipping rate to the general deposition process. The first, by de Gennes, placed a constant upper bound on the maximum deposition speed; the bound is due to the interfacial energies at the meniscus given

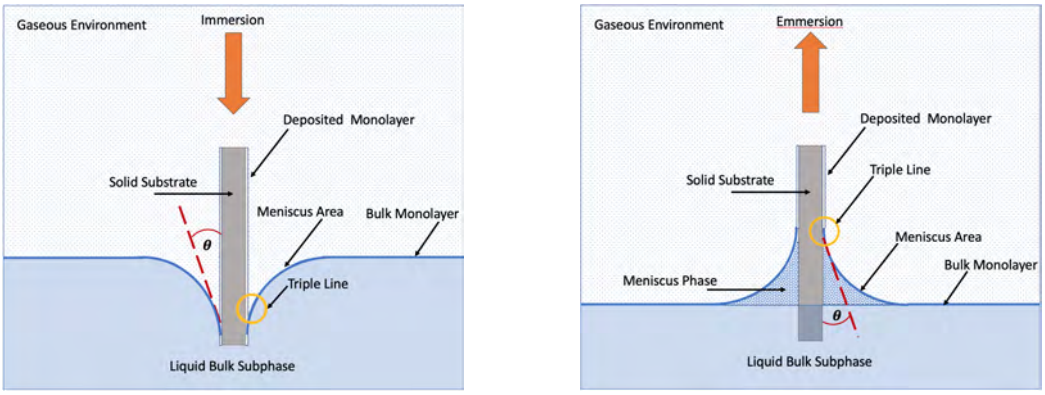

(a) Immersion of substrate through the water-air interface.

(b) Emmersion of the substrate through the water-air interface.

Figure 2.5. Meniscus dynamics during dipping process. The angle of contact is shown in red.

certain values for contact angle, surface pressure in the trough, and dynamic viscosity of the system [62]. Although this bound agreed with experimental results at the time, it was later contradicted when deposition rates nearly twice those predicted by de Gennes were observed given different parameters [59].

A subsequent model by Buhaenko and Richardson [63] focused on the free energy present in the system located at the triple line (shown in Fig. 2.5). In this model, the ratio of force exerted by the substrate on the sample holder to the perimeter of the triple line around the substrate is proportional to the contact angle of the triple line. That is,

$$-\left(\frac{F}{P}\right) = \gamma cos(\theta)$$

where F is the force of the substrate on the holder, P is the perimeter of the triple line around the sample, γ is surface free energy, and θ is contact angle between the subphase and substrate. The result predicts different forces and different contact angles for substrate immersion versus emersion [63]. This model was expanded on by Egusa et al. [64], and experimentally demonstrated that deposition is accompanied

by dynamic interfacial forces, deposition does not occur when interfacial forces are constant, and there exist interfacial forces for which deposition does not occur.

Finally, a model by Blake and Haynes related dipping speed to the activation energy required to move the contact three-phase line from one location to the next across the substrate [65]. This model was expanded by Petrov [66] to explain the variation in contact angle and transfer speed throughout the dipping process by placing LB deposition in the context of molecular dynamics and hydrodynamics. Petrov's model represents the connection between macroscopic properties (θ_E the angle of contact at equlibrium, γ the surface tension, μ the viscosity of the liquid, and ρ the density of the liquid) and microscopic properties (k the rate of adsorption/desorption, λ the mean distance between nearest nucleation sites, and n the number of adsorption sites) [66].

Other experimental data confirms that the rate at which the substrate is dipped has an important role in the deposition process, where faster dipping has a better effect on layers [59]. This effect is partially attributed by Mahnke et al. to meniscus oscillations and instability at the three-phase interface during transfer of the thin film from the subphase surface to the substrate [67], and by Grundy et al. to disturbance of the ML while the substrate is submerged in the subphase [59]. Within literature, various dipping rates have been reported, from 1 mm/min to 120 mm/min [4,6,59,67].

Emphasizing consistent dipping rate and dipping angle as fundamental to LB experiment design agrees with well established theory and experiment. Furthermore, Petrov's model unites the two by showing that the dipping velocity is a function of the angle of contact [66]. The automated LB deposition system discussed in the next section seeks to emphasize control over these two parameters through hardware and software engineering.

2.2.2 Approach to Automating Langmuir Blodgett Deposition

The KSV Minitrough is "a computer controlled and user programmable Langmuir-Blodgett instrument for automated Langmuir film experiments and for unsupervised

Figure 2.6. Automated Langmuir Blodgett Trough Deposition System. Although the metal base and barrier arms are original to the KSV Minitrough system, the white dipping trough, dipping assembly with arm and sample holder, and microcontroller mounted on the back of the dipping assembly are specific to this project. Image by Sarah Dale.

deposition of normal multilayers onto solid substrates [68]." The original system released in May 1991 required a Windows 3 operating system and was controlled through serial RS232C communication passed to a separate control unit. In addition to its functionality for thin film deposition, the KSV Minitrough also featured accessories to study the compression dynamics of thin films on a liquid subphase.

By 2018, the KSV Minitrough system in IUPUI's Physics Department consisted of the metal trough frame, two trough barriers for surface compression, a custom trough with viewing window (but without the reservoir used for casting thin films onto substrates) and the original KSV control unit. In order to bring the system back to functionality for use in LB deposition, a new trough with a reservoir, an automated sample dipping mechanism, and software compatible with both the original control unit and Windows 7 were required. Future implementation of an automated

syringe pump to deposit the thin film solution onto the subphase in the trough and an enclosure containing the entire system in a nitrogen environment will further increase the system's ability to produce consistent, high quality thin films.

In the following sections, the fabrication of a new, custom dipping trough, development of a dipping mechanism for the trough, and the creation of python and LabVIEW software to integrate the various components are discussed. Explanations for significant design decisions and implementation details for sample fabrication are provided.

Fabrication of Langmuir Blodgett Trough

A new dipping trough was machined from a single block of 2.75"x7.25"x16" Delrin® acetal plastic. Acetal is a thermoplastic and engineering resin. It is easily machined, hydrophobic with low moisture absorption, and non-reactant with various organic solvents [69].

A complete schematic of the trough design was created by measuring the original flat-bottomed trough accompanying the KSV Minitrough system, then calculating the necessary modifications for a trough with a dipping reservoir. The original dipping trough had a "240 mm x 75 mm effective film area" [68] with outer dimensions of 11.75" x 3". The outer dimensions are constrained by the metal base which holds the trough. The new design maintained the original dimensions, with the exception of adding a 1.15" x 0.73" x 2" well centered in the trough base to allow submersion of a sample substrate. These well dimensions were specifically chosen so that standard 1" glass laboratory slides could be used as a substrate for deposition.

The acetal work piece was trimmed to within 1" of the final measurement using a vertical band saw. The work piece was then checked for squareness and milled using a 3/4" roughing end mill to remove the bulk and square the sides, and a Sandvik Coromant 3" shell cutter to finish the surface.

(a) Bulk material was removed from the work piece using the shell cutter tool. A large quantity of acetal chips are visible on the work piece mounting block.

(b) The top of the trough containing the film area was created using pocket milling with an end mill tool.

Figure 2.7. Milling the custom Langmuir-Blodgett trough with dipping well for the automated deposition system. Photo credit: Aaron Mosey

The top film area was pocket milled using a 1/2" 2 flute end mill, and the well was pocket milled using a 1/4" ball end mill. After milling was completed, the entire piece was hand polished using a high-grit sandpaper to remove residual surface texture. The trough was then cleaned using acetone, methanol, isopropanol, and DI water, and installed in the trough base. The completed custom trough is shown installed and ready for use in Figure 2.6.

Design and Construction of Automated Dipper

Initial PVDF thin film samples were made using a hand-dipping method for LB deposition, where tweezers were used to vertically immerse and extract the sample into and out of a polymer thin film floating on a subphase of 18 MΩ MilliQ H_2O in a 50 mL beaker. Although excellent thin films are possible with this approach, the quality of the thin films vary greatly with many samples failing to demonstrate crystal structure. One such failed sample is shown in Figure 2.12.

The issues with hand fabricating samples lie in human error and variability. When using a hand-dipping method, it is impractical to constantly measure the dipping speed and difficult to maintain a constant dipping speed over time. Hand-dipping methods also do not allow for calibration of the dipping angle or a consistent dipping angle. By automating the process, consistent dipping rates are guaranteed and calibration of the dipping angle is easily controlled.

A commercially available linear actuator of the kind used in CNC mills was chosen to form the main component of the dipping mechanism. The linear actuator has a 100 mm travel length and a pre-mounted stage that forms the base of the dipping arm. The dipping arm consists of a 21 cm length of threaded rod and is mounted to the linear actuator's base using the pre-exisiting nut assembly on the base. The dipping arm terminates in a clip to hold the sample at a constant angle relative to the subphase surface.

The linear actuator is driven by a NEMA-17 stepper motor (see data sheet in Appendix C.1), and controlled by an Arduino Uno v2 microcontroller with an Adafruit Motor/Stepper/Servo Shield v2.3. The stepper motor is mounted on the linear actuator with a rubber vibration damping collar between the motor and actuator to reduce noise transferred from the motor to the trough and dipping arm. Additional vibration damping methods are recommended.

The Adafruit Motor Shield implements a TB6612FNG driver IC (see data sheet in Appendix C.2) to control the motor, and offers a python library specifically for use with the motor shield. The Arduino Uno microcontroller runs embedded python code (see Appendix section A.1 for code) and communicates with the LB trough through a LabVIEW program which coordinates all aspects of the deposition system.

The final dipping mechanism with the stepper motor operating in single step mode is capable of generating dipping speeds of 114 mm/min, 187.5 mm/min, 246 mm/min, and 300 mm/min. Four of the five dipping rates are well in excess of those reported in literature, and the stepper motor produces considerable vibrational noise

when running at top speed. However, the motor shield is capable of implementing microstepping to control the motor speed and produce smoother motion.

Development of NI LabVIEW Drivers for System

The original manual for the KSV minitrough system states "[b]ecause each device includes its own microprocessor, the computer sends only some high level commands to them (for instance -move with certain speed- or -go to certain position- and so on). All devices are listening to every message, but they become active only when they recognize their own address [68]."

Using this information, a system architecture for the automated LB system was developed that integrated the various custom components with manufacturer components using custom LabVIEW drivers in place of, or in conjunction with, the original microcontroller firmware as needed. This architecture is shown in Figure 2.8. The main LabVIEW VI, Dipper SubVI, LB Trough SubVI, and Python Firmware as shown in Figure 2.8, are all software created specifically for this project and the code may be found in Appendix A.3. Microcontrollers are denoted where relevant, and significant hardware elements are represented by cubes in the flow diagram.

The current generation of KSV Nima LB troughs use the same communication protocols as those from the 1990s, and a modern copy of the control software was obtained from the distributor. The modern control software eliminated the need for a Windows 3 operating system, but did not allow for integration of custom-built components such as the dipper arm.

Instead of attempting to implement the manufacturer control software with the custom components, the Portmon COM port sniffer was used to capture all of the commands written to the KSV control unit during the startup, control and shutdown procedures of the KSV control unit. The commands were intercepted as pure hex values, and initially there was no direct mapping between output values from the trough and the hex commands. However, a spontaneous insight showed that the hex

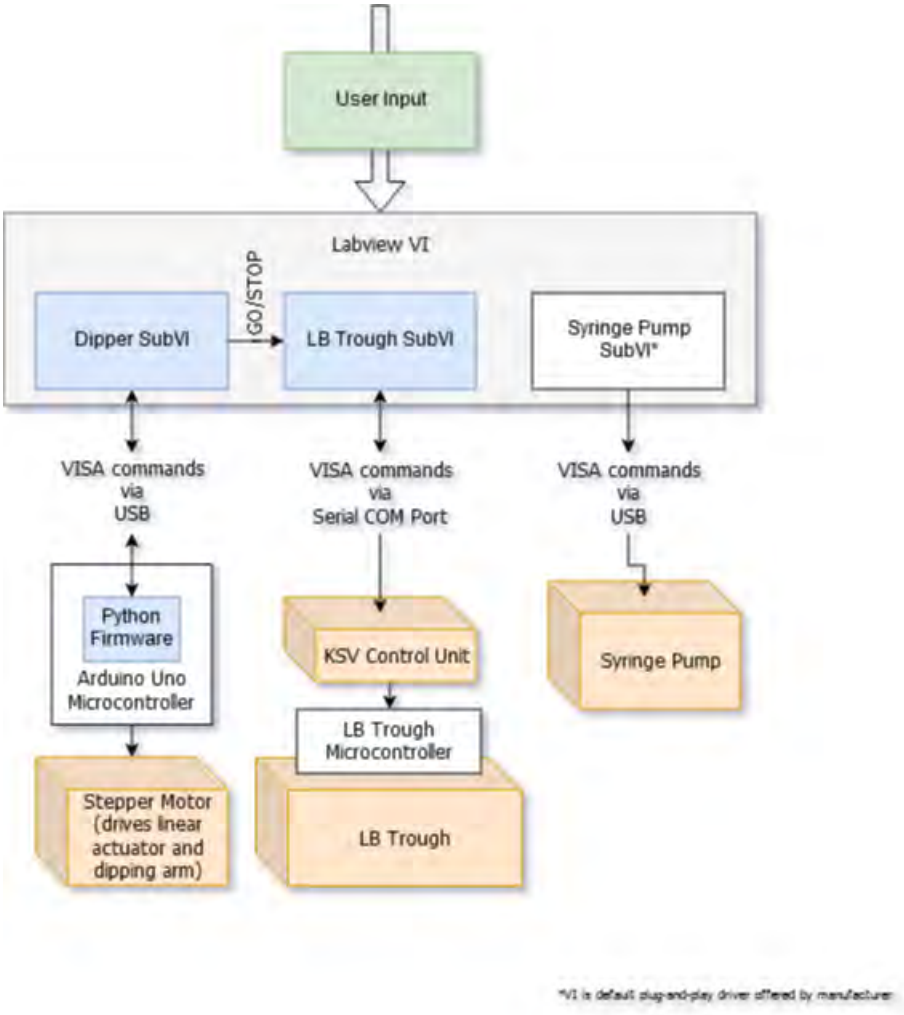

Figure 2.8. System architecture for automated deposition system. The Dipper SubVI, LB Trough SubVI and Python Firmware shown in blue boxes were created specifically to connect the custom components with the KSV Control Unit and the Syringe Pump.

commands were merely ASCII characters whose numerical values had been converted to hex, these hex values treated as ASCII characters to be readable as strings, and then converted to hex values again for transmission. In practice, this means that to obtain the trough barrier position values as output by the KSV control unit, each transmitted position value read from the KSV control unit requires a four-step

de-encryption process in LabVIEW (HEX → ASCII interpreted as HEX → ASCII → LabVIEW Integer).

These captured commands were then implemented in LabVIEW to create a program with identical functionality to the manufacturer control software. The manufacturer control software interface is shown in Figure 2.9, and the main LabVIEW VI shown in Figure 2.10 was modeled after it. Additional adjustments were made to the error checking, rate of transmission, and XON/XOFF settings in LabVIEW to enable reliable communication between the laboratory computer and the KSV control unit.

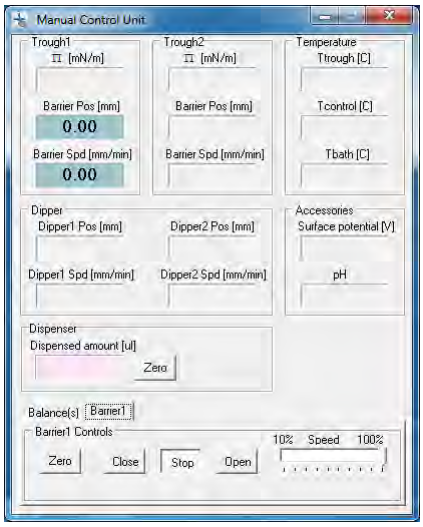

Figure 2.9. KSV NIMA Manufacturer software for manually controlling LB trough.

Similar work was required to create the LabVIEW driver for the automated dipping system. Communication was established between the Arduino Uno microcontroller and LabVIEW using NI VISA protocols. A library of string commands was created in the LabVIEW driver, sent through the VISA communication interface, and parsed by the custom python firmware on the Arduino Uno.

After creating the independent LabVIEW drivers, each was integrated into a single LabVIEW program as subVIs. This allows for simultaneous, automated control of the system through the single computer-based visual user interface shown in Figure 2.10.

When used in the fully-automated mode, the "Zero", "Close", "Stop", and "Open" buttons on the "Trough Settings Tab" in Figure 2.10 are deactivated, allowing the VI to fully control the system.

To run an experiment, the user follows the instructions on the LabVIEW front panel, enters the necessary parameters, and starts the system.

This restores full functionality of the automated deposition system.

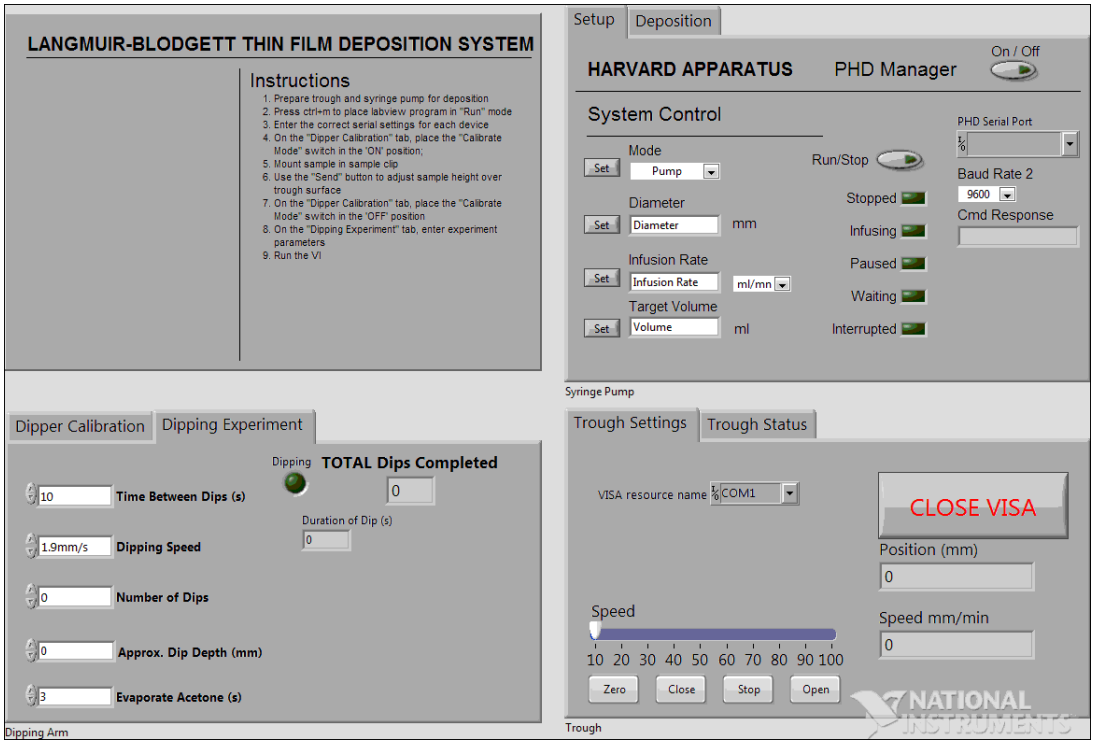

Figure 2.10. LabVIEW front panel controlling automated LB system. Top L: User instructions for the system. Top R: Syringe pump driver and settings. Bot L: Dipper experiment controls Bot R: LB Trough controls.

2.2.3 PVDF-HFP Thin Film Deposition

It is imperative for LB thin film deposition that the trough, barriers and workspace be as clean and dust free as possible. Any debris, grime, oils, or other foreign matter interferes with the uniform formation of thin films [57]. The first step to depositing

excellent thin films is to clean the trough and barriers using acetone, methanol, isopropanol, then 18MΩ MilliQ H_2O and using a kim wipe as necessary to remove any debris.

Once the trough, barriers, and general workspace are clean, the barriers are placed on the trough and the trough is filled with 18 MΩ MilliQ H_2O until the meniscus rises above the trough edge height by at least 3 mm. The barriers are then slowly closed, and any debris which has landed on the subphase surface is removed with an aspirator at the barrier edges as it accumulates. After the subphase is free of debris, the barriers are opened and water is removed from the trough with a syringe until the subphase surface is just even with the top edge of the trough.

A volatile solution with a mass fraction of 0.05% PVDF-HFP is prepared by dissolving powdered PVDF-HFP in acetone heated to 80°-125°C until the powder is completely dissolved and the solution has reached the boiling point. The choice of solvent greatly affects the formation of the thin film on the subphase surface [70]; various ratios of acetone to *N*, *N*-dimethylformamide (DMF) [3, 5, 6, 13, 38, 70] and dimethyl sulfoxide (DMSO) [8, 71, 72] are among the most commonly used. Various other solvents used with PVDF include *N*-methyl-2-pyrrolidone (NMP) [4,70], diethyl carbonate [41], and methyl ethyl ketone (MEK) [7, 70].

The addition of hydrated salts such as $Mg(NO_3)_2{\cdot}6H_2O$ and $Ca(NO_3)_2{\cdot}4H_2O$ to the solution has been shown to improve the percentage of β-phase at the cost of an increase in thin film surface roughness [38, 73, 74]. In the pursuit of more uniform thin films, additives were omitted from this study.

The PVDF-HFP in acetone solution is allowed to cool to room temperature, then deposited on the subphase surface with a pipette at the ratio of 1 mL of solution to 500 cm^2. During this deposition process, approximately 90% of each pipette drop is lost in the subphase, and the remaining 10% floats on the subphase surface in the trough forming a ML thin film [28]. As PVDF-HFP is not a true amphiphile, the ML thin film on the subphase surface is not a true ML; it demonstrates a varying thickness approximately 3x the molecular diameter of the PVDF copolymer [40].

The trough is then left undisturbed for 15 minutes to allow the solvent to fully evaporate and the surface to become still.

A substrate with or without a bottom electrode may be cleaned in the multi-step solvent process a final time before deposition if it has become dirty or damaged between electrode deposition and LB deposition. The substrate is then mounted on the dipping arm, and parameters are entered in the LabVIEW VI controlling the system. The main parameters are number of dips, dipping stroke depth, dipping speed, and trough barrier speed. The number of dips controls the final number of monolayers (ML) deposited on the substrate, dipping stroke depth controls the final sample size, dipping speed and trough barrier speed coordinate to help maintain a constant surface tension and ensure even deposition on the substrate surface.

The actual number of ML transferred during deposition varies widely. Kleim et al. report a range of 0.97 ML to 1.276 ML (0.485 nm to 0.638 nm) transferred on average per deposition as determined by dividing by nominal PVDF-TrFE monolayer thickness [19]. Ducharme et al. report an average of 1.78 $\pm$ 0.07 nm deposited per ML for the same nominal PVDF-TrFE thickness based on work by Bai et al. [8, 28].

A good quality PVDF-HFP thin film of only 5 ML is clearly visible to the naked eye through its iridescence. This is demonstrated in Figure 2.11, where the bottom edge of the sample is PVDF-HFP thin film deposited on glass, and the edge between the glass and the metal electrode is clearly visible due to the PVDF-HFP thin film translucence. The pink and bluish stripes in Fig. 2.11 are the iridescence of the thin film overlapping the glass and electrode. For comparison, a poor quality film of 60 ML is presented in Figure 2.12; there is no iridescence and the white flecks across the thin film surface hint at an inconsistent transfer ratio from subphase to substrate.

Between each dip, the sample is allowed to completely dry. Drying times have been reported to be as long as 15 minutes [6], but through observation it was found that as PVDF-HFP ML are deposited the sample becomes hydrophobic. This hydrophobicity allowed dry times to be as short as 90 seconds.

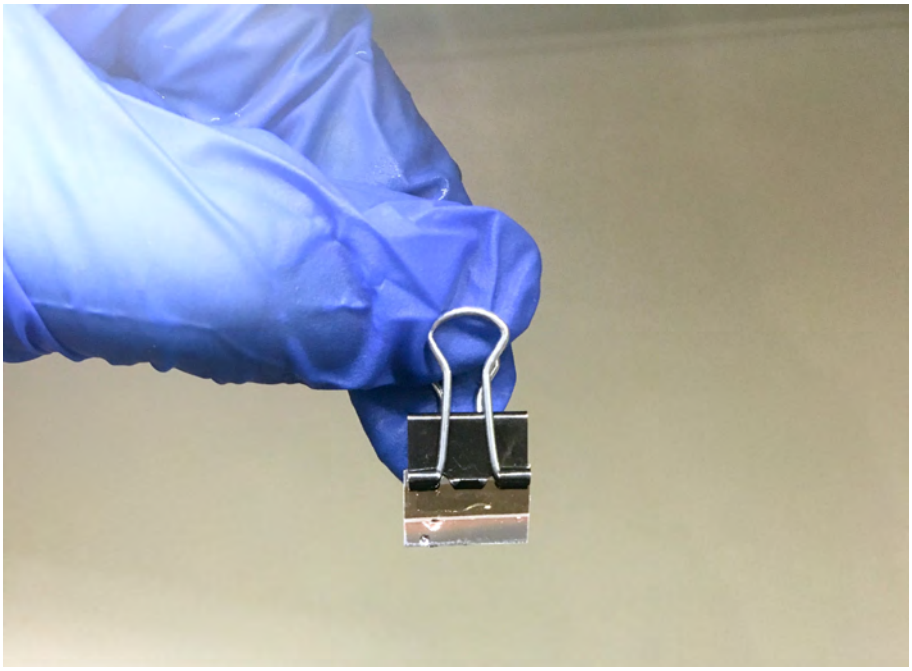

Figure 2.11. The iridescence of the thin film on the glass substrate and metal electrode is clearly visible. Note that the liquid drops on the sample surface indicate the sample is not yet hydrophobic.

When the desired number of MLs has been achieved, the sample is removed from the LB trough and prepared for the deposition of a top electrode as discussed in Section 2.1.2. After the deposition of the top electrode, the sample is ready for characterization.

Figure 2.12. A 60 ML PVDF-HFP thin film on Si substrate (no electrode) fabricated using the hand-dipping method. The white flecks are attributed to uneven evaporation from the subphase surface. The lack of irridesence is a clear indicator of an absent crystal structure. During ferrroelectric testing, this sample behaved like an insulator.

3. THIN FILM CHARACTERIZATION

To determine if the methods implemented in the automated LB deposition system were successful, characterization of samples made with and without the system was undertaken using a variety of methods. Criteria for sample characteristics are high electric coercivity, larger crystal domain sizes, dominant β-phase crystal structure, and more uniform surface morphology. The data for these criteria were collected via ferroelectric measurement, atomic force microscopy (AFM) and scanning electron microscopy (SEM) respectively.

3.1 Ferroelectric Measurements

Ferroelectric capacitors are frequently characterized by the electric field strength required to reverse the polarization of the ferroelectric crystal; this is the sample's electric coercivity. Determining the electric coercivity of a sample requires exposing the sample to an oscillating electric field, then measuring the change in sample current as a function of the oscillating field.

The measured sample current has three components: the nonlinear polarization-inversed current density originating from the polarization of electrets J_n, the linear polarization current density originating from the bulk conductivity of the sample J_l and leakage current originating from charging the capacitive device structure J_σ [37, 75]. This can be summarized as

$$J = J_n + J_l + J_\sigma$$

where $J_n = A\frac{dP}{dt}$ with A the area of the sample electrode and P the polarization of the dipoles in the electrets, $J_l = C\frac{dV}{dt}$ with C the capacitance of the sample and V the applied voltage, and $J_\sigma = \frac{V}{R}$ with V the applied voltage and R the resistance of the

sample [37, 75]. To obtain the polarization value of the dipoles, the J_l and J_σ terms must be subtracted from the measured current, and then the measurement must be integrated numerically.

A common approach to obtaining an electrical hysteresis measurement is the Sawyer-Tower circuit. First proposed in 1930 to determine the dielectric constant of Rochelle Salt, the original Sawyer-Tower circuit consisted of a voltage divider, the sample under test, a capacitor to synchronise the phase of the measured signal with the applied signal and a cathode ray tube to view the output voltage of the sample [76]. The circuit was connected to a 130 V, 60 Hz power line and the resulting hysteresis loop was displayed on the cathode ray tube as a function of applied voltage vs measured charge as shown in Figure 3.1 [76].

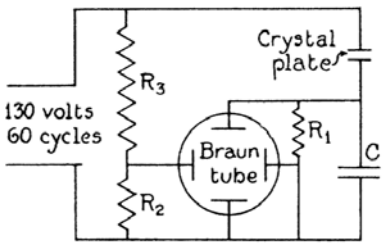

Figure 3.1. Original Sawyer-Tower circuit to determine the dielectric constant of Rochelle Salt [76]. In the circuit shown, $R_1 = 0.45$ MΩ, $R_2 = 3.18$ MΩ, $R_3 = 31.8$ MΩ, and $C = 0.7$ Mf. Figure from [76].

The Sawyer-Tower circuit continues to be modified by updating the equipment (e.g. cathode ray tubes have been replaced by digital oscilloscopes and the power line has been replaced by a voltage source and/or function generator) and through the addition of various filters to compensate for leakage current, integrate the measured output, and to compensate for systemic errors arising from hardware. [35, 36, 77–79], It would seem that the Sawyer-Tower circuit is infinitely customizable depending on the needs of the experimenter, up until the point when the experimenter requires a measurement system independent of frequency.

The Sawyer-Tower circuit by definition contains an oscillating voltage, sometimes a sine wave [37], sometimes a triangle wave [80], possibly even a pulsed wave [35], but the measurement always occurs at some known frequency. Although the use of an oscilloscope prevents measurements at extremely low frequencies due to the internal impedance of the oscilloscope [78], this issue may be avoided by adding a voltage follower [78] or automating the measurement through LabVIEW [75, 81].

Even after the Sawyer-Tower circuit has been revised to adjust for the limitations of oscilloscopes, hysteresis measurements of FE materials have a well-known dependency on frequency [82]. Low-frequency measurements require corrections for trapped charges, corrections which can be nearly impossible to make [19]. A solution to this problem is to omit frequency entirely by evaluating the sample under an applied electric field after charge displacement has stopped and when it the sample has achieved equilibrium. This equates to abandoning the Sawyer-Tower circuit.

An approach to ferroelectric measurement without a Sawyer-Tower circuit was proposed by Kliem et al. to distinguish between intrinsic and extrinsic switching mechanisms [19]. Kliem et al. show that any frequency-based measurement cannot consist solely of dipole-based polarization and present a strong argument for why FE thin films should be analyzed from the perspective of intrinsic switching.

Several practical reasons also promote Kliem et al.'s two-pulse method. First, software based experimental systems can be relatively cheap to obtain [81], and at first glance Kliem et al.'s two-pulse measurement approach—recommending 50 minutes to obtain a single data point in a hysteresis loop which may contain dozens of points–seems uniquely suited to a software-based implementation. Second, a software based implementation obviates the need for much of the hardware correction required by Sawyer-Tower circuits, resulting in a more accurate measurement. Finally, a software implementation removes the constraints on sample size inherent to hardware sampling approaches while maintaining a flexible structure for implementing digital filtering techniques.

Therefore, to gain complete control of the ferroelectric characterization, a system was developed to implement the two-pulse method in LabVIEW and use the Keithley 6487 Picoammeter/Voltage source as both the voltage source and to measure the current. This work is discussed in detail in Section 3.1.1.

3.1.1 LabVIEW Implementation of Two-Pulse Method

The algorithm presented by Kliem et al. is straight forward:

1. Apply a voltage pulse of V_i to the sample until the measured current reaches a steady state. Record the measured current values as $Q_1(t)$.

2. Turn off the electric field and allow the sample to relax until measured current reaches a constant value (i.e. zero current).

3. Reapply the voltage pulse of V_i to the sample until the measured current again reaches a steady state. Record the measured current values as $Q_2(t)$.

4. Subtract $Q_2(t)$ from $Q_1(t)$ and divide by the area according to the relation

$$P(t) = \frac{1}{A}(Q_1(t) - Q_2(t))$$

5. Update V_i to the next voltage value V_{i+1}. Repeat from (1.) with $V_i = V_{i+1}$ until n points have been obtained.

The voltage values are obtained by sampling a voltage wave form based on the desired number of points in the hysteresis loop. For example, a 2 V peak-to-peak triangular wave centered at 0 V may be sampled evenly every 0.1 V to obtain a hysteresis loop containing $n = 40$ points.

After the polarization values $P(t)$ are obtained, they are averaged to obtain a single value. The electric field $\mathcal{E}$ is obtained by dividing the voltage V by the sample thickness ϵ:

$$\mathcal{E} = \frac{V}{\epsilon}$$

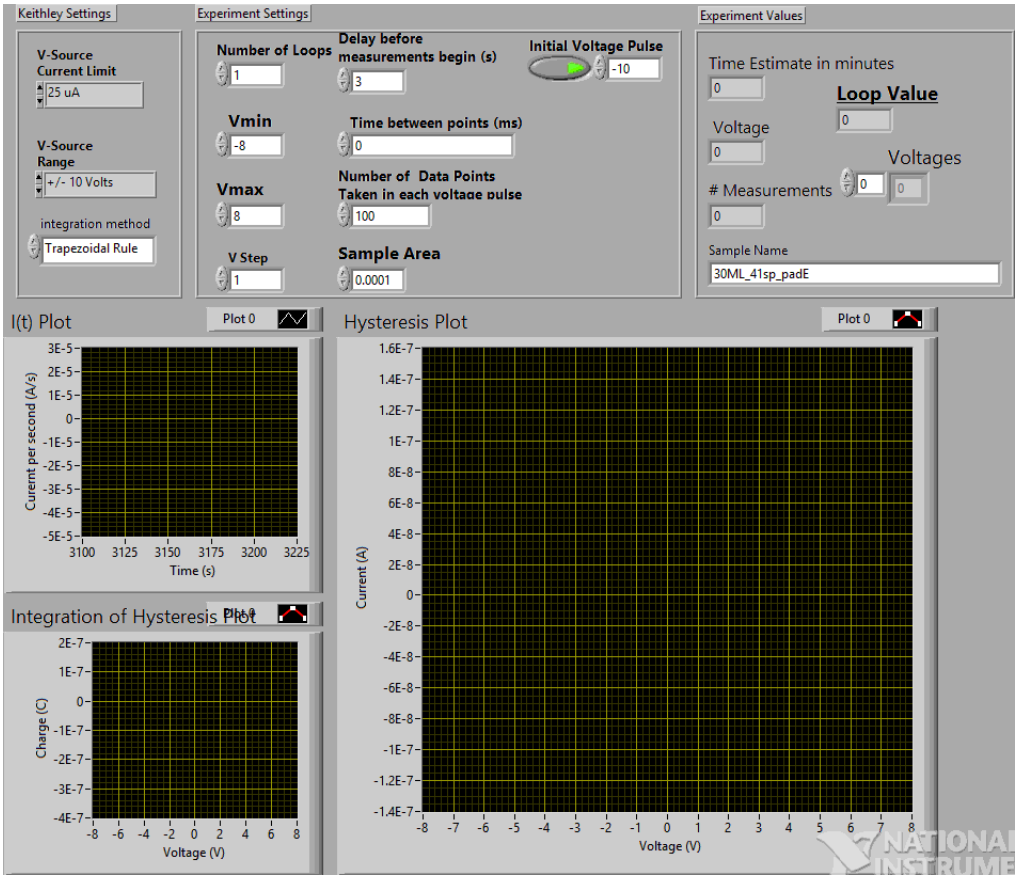

Figure 3.2. Front panel of LabVIEW Electrical Hysteresis Measurement.

. The hysteresis loop is obtained by plotting the polarization values against the electric field values as shown in Figure 3.6.

The LabVIEW implementation accepts user inputs to determine the maximum and minimum applied voltage values, the size of the voltage step, and the amount of time to wait for the sample to reach a steady state in terms of the number of samples taken during each voltage pulse. After accepting input values, the program creates an array of voltage values to be passed to the voltage supply, and enters a loop where each voltage value is applied according to the algorithm described above, and the resulting current measurements is simultaneously integrated to obtain the polarization and displayed on a plot to the user as time vs. current and applied

voltage vs polarization. The plots are updated as each data-point is completed to aid in experimental troubleshooting and on-the-fly data analysis. After each polarization data point is obtained, the raw current data, voltage data, time data, and integrated current values are saved to an array to be written to a text file after the experiment ends. The text file also contains the sample name as provided by user input and relevant parameters and constants used during polarization determination (e.g. sample size, sample thickness).

Additional LabVIEW implementation features include the ability to polarize the sample with a known voltage before the hysteresis measurement begins, control over basic picoammeter/voltage source settings, and a rough estimate of how long the program will run based on the estimated time it takes to complete the required number of samples from the received current signal. The front panel for the system is found in Figure 3.2. The code is in Appendix section A.2.

The Keithley 6487 Picoammeter/Voltage Source features communication via GPIB allowing SCPI commands to be written to the picoammeter directly from the LabVIEW interface. LabVIEW plug-and-play drivers available for the picoammeter from Keithley aid in establishing a robust communication protocol. The picoammeter/-voltage source is capable of applying 0 V to ±250 V, and sampling current at a rate of 1000 samples/second [83]. Adjusting the sampling rate allows for better control of noise in the system at the cost of information about how the sample reaches steady-state behavior.

3.1.2 Electrical Hysteresis Measurement

Electrical measurement of samples requires that the sample be placed into a circuit with the Keithley ammeter/voltage supply as shown in Figure 3.3. Although the samples have top and bottom electrodes, connecting these to the ammeter while minimizing electrical noise during measurement presented a challenge due to the lack of standard electrical connectors on a Si or glass substrate. To solve this connectivity

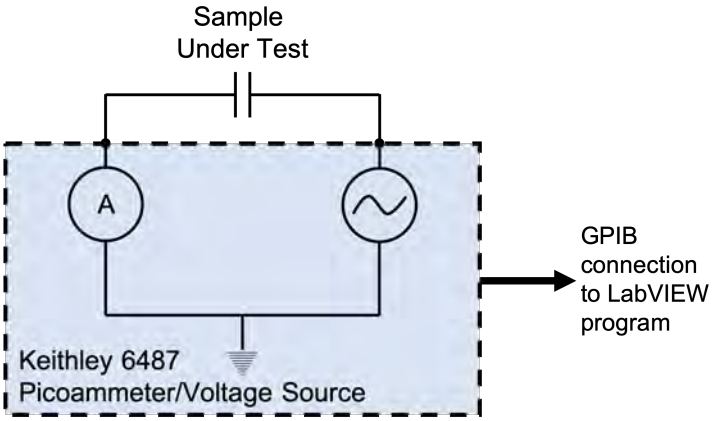

Figure 3.3. Circuit for ferroelectric measurements. This circuit is recommended in the Keithley 6487 manual for ohmic measurement. The GPIB connection to the computer passes commands to the voltage source from the LabVIEW program and collects data from the ammeter.

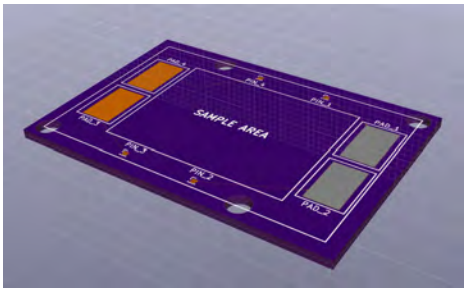

(a) Computer rendered illustration of board design in KiCad software.

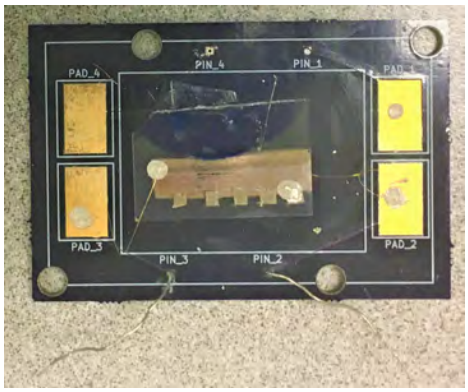

(b) Actual board with mounted sample. Au wires connect the top electrode and bottom electrode of the sample to the conducting pads on the PCB.

Figure 3.4. Custom printed circuit boards (PCB) for ferroelectric measurements of capacitive samples. Using a PCB with large conducting pads enabled better electrical connections between the sample and the ammeter/voltmeter, reducing measurement noise.

issue, 0.05 mm gold wire and conductive silver paint connect the sample to a custom printed circuit board (PCB) populated with standard connectors. This helps limit the number of temporary electrical connections required for each measurement, greatly reducing noise and interference. Figure 3.4(a) shows the PCB design, and Figure 3.4(b) shows a sample mounted on the board ready for measurement. The PCB was designed using the open source package KiCad and fabricated by the PCB house Osh Park.

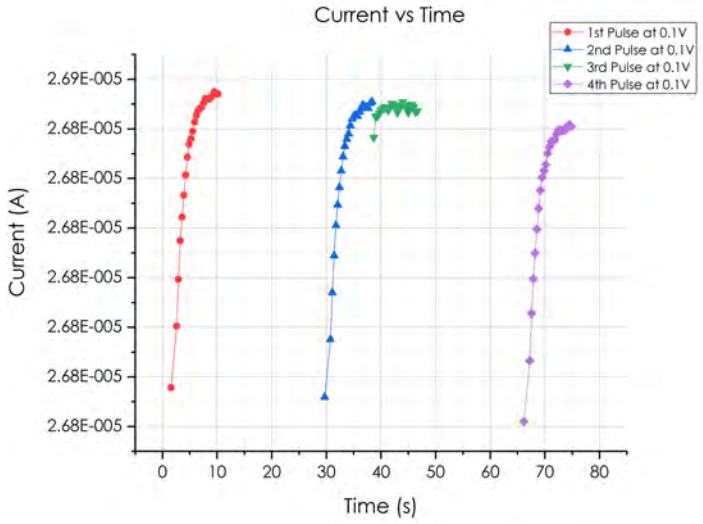

Figure 3.5. Current measurements from four applied voltage pulses of 0.1V. The sample was allowed to fully discharge between pulses 1 and 2, and between pulses 3 and 4.

Ferroelectric fatigue directly affects the quality of the electrical measurement. This is seen in Figure 3.5; four pulses of 0.1 V were applied to a sample and the sample was allowed to fully discharge between pulses one and two and between pulses three and four. Since the current was measured continuously, the decay of the ferroelectric thin film is clearly visible in the decreased magnitude of the maximum current measured during each pulse.

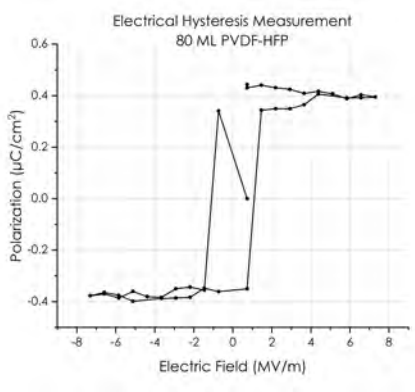

(a) Electrical hysteresis measurement for auto-dipped 80 ML sample.

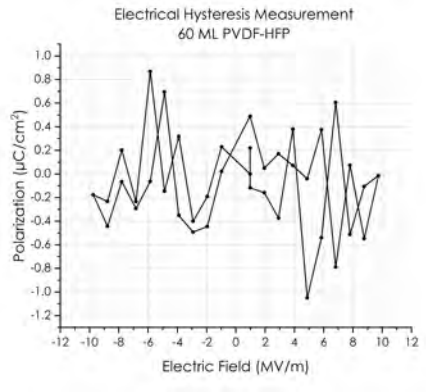

(b) Electrical hysteresis measurement for hand-dipped 60 ML sample.

Figure 3.6. A comparison of identical electrical measurements between an auto-dipped sample and a hand-dipped sample. While the auto-dipped sample clearly demonstrates hysteresis, the hand-dipped sample represents only the system's noise.

An electrical measurement identical to the one implemented in Figure 3.6(a) is implemented in Figure 3.6(b), with remarkably different results. The hand-dipped sample electrical measurement represents the noise in the system, with no visible hysteresis. Neither of these samples were able to be characterized by a Radiant 6000B ferroelectric system; each sample returned an error of too much current due to the ratio of thin film thickness to electrode area. Removing hardware limitations enabled data gathering and analysis of samples formerly neglected.

3.2 Additional Characterization

3.2.1 Atomic Force Microscopy

Atomic force microscopy (AFM) is commonly used to evaluate thin film surface roughness and domain phase information. In Figure 3.7, AFM data from two samples is presented–one hand-dipped sample and one auto-dipped sample–with noticeable

difference between the two. The grain size in the auto-dipped sample is fairly typical of thin film structures, while the hand-dipped sample has no discernible grain structure at all.

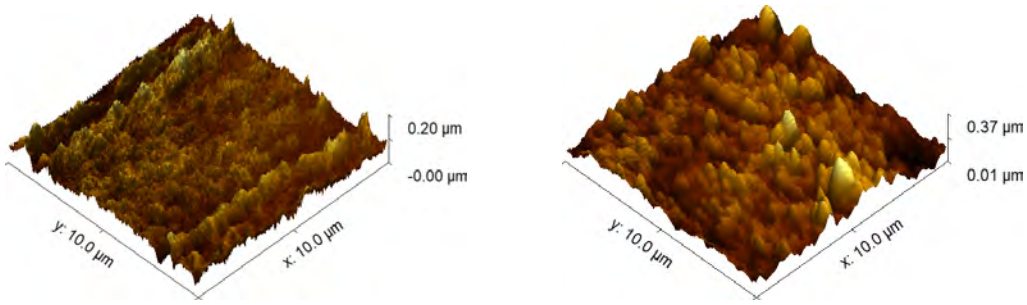

(a) 60 ML hand-dipped sample. The ridges parallel to the x-axis area feature of the sample and may arise from meniscus oscillations [67].

(b) 150 ML auto-dipped sample. Distinct grains in the thin film are visible.

Figure 3.7. Comparison of AFM data for a hand-dipped and auto-dipped sample.

In Figure 3.7(a), the hand-dipped sample has stripes parallel to the x-axis; these stripes may be due to the meniscus oscillations as observed by Mehnke et. al. in LB thin films of arachidic acid on hydrophobized glass [67].

3.2.2 Scanning Electron Microscopy

Scanning electron microscopy was used to evaluate an auto-dipped sample and a hand-dipped sample at 2.00 kV and x8,500 magnification. The surface morphology of the auto-dipped sample shown in Figure 3.8(a) is uniform with a dense thin film structure compared to the hand-dipped sample shown in Figure 3.8(b). The hand-dipped sample has wrinkle-like surface features that hint at how the lack of surface area control may affect deposition.

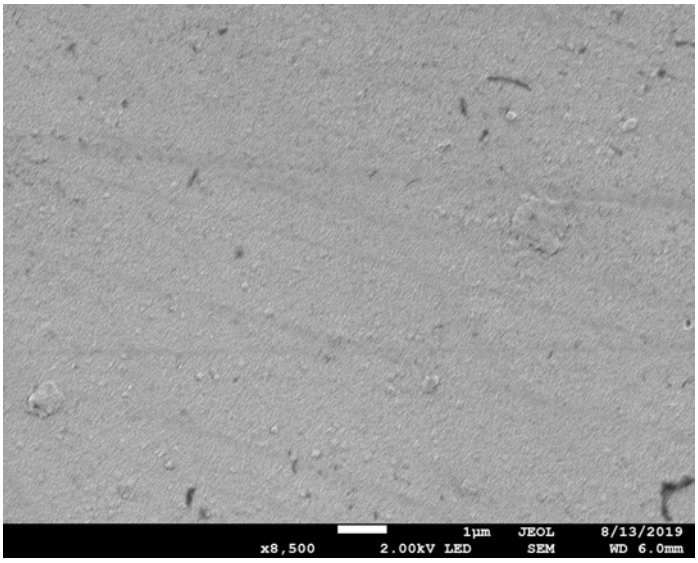

(a) 60 ML Auto-dipped Sample.

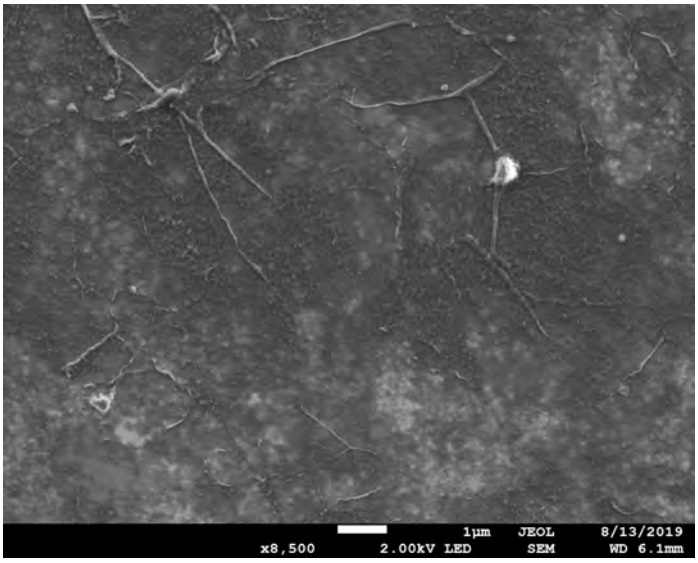

(b) 60 ML Hand-dipped Sample.

Figure 3.8. SEM data taken of a 60 ML PVDF-HFP on Si sample.

3.2.3 Miscellaneous Characterization Methods

To truly confirm that a sample contains a high percentage of β-phase, at least two complementary characterization methods (e.g. X-ray diffraction (XRD) and fourier

transform infrared spectroscopy (FTIR), XRD and differential scanning calorimetry (DSC)) must be implemented due to the overlap in characteristics between the various phases [9, 32].

It is worth noting that the presence of the copolymer in PVDF-HFP should influence numerical values reported from the methods describing PVDF below. This is clearly seen in the data for the PVDF XRD peak compared to the XRD peak for PVDF-HFP. However, since the unit cell and overall crystal structure remain largely consistent across PVDF and its copolymers, these approaches should continue to be valid for determining new constants particularly for PVDF-HFP.

Accordingly, a selection of several common characterization methods are presented in the following sections to provide context for a discussion of future work.

2D X-Ray Diffraction

PVDF and PVDF-TrFe exhibit a quasi-hexagonal close packing structure [43, 84]; it is reasonable to assume that PVDF-HFP demonstrates a similar structure.

Previously reported values for the PVDF-HFP β-phase(1 1 0) XRD peak are 20.6° 2θ [5] and 20.8° 2θ [38], slightly larger than the reported value of 20.26° 2θ for PVDF alone [9, 32].

The Wide Angle X-ray Diffraction (WAXD) peaks for PVDF-HFP have been shown to shift due to the ratio of the copolymer to the polymer, where a higher concentration of the copolymer corresponds to a larger 2θ angle [39, 43]. The copolymer has a similar effect on XRD peaks, explaining the slight difference between the various reported data.

Reported peaks exist at 17.7°, 18.3°, and 19.9° 2θ for the α-phase and at 18.5°, 19.2°and 20.0° 2θ for PVDF [9]. However, given the soft nature of the polymer structure and the effect the copolymer plays on spacing, it is reasonable to assume that other accepted values for the dominant phase peaks exist. This variability emphasizes the need for additional methods to confirm crystal phase.

Fourier Transform Infrared Spectroscopy

Fourier transform infrared spectroscopy (FTIR) is a popular choice for evaluating the percentage of various phases in PVDF thin films [9, 31]. Data may be analyzed using the expression for the four symmetry species

$$\Gamma = 5A_1(\mu'_b, \alpha'_{bb}, \alpha'_{cc}) + 2A_2(\alpha_{ac}) + 3B_1(\mu'_c\alpha'_{ab}) + 4B_2(\mu'_a, \alpha'_{ab})$$

where μ'_i represents the dipole moment and α'_{ij} represents the transition polarizability [31]. Therefore, analysis of FTIR data confirms the presence of various phases in the PVDF structure, but does not allow a quantitative determination of the percentage of phase present in the structure [44].

Furthermore, while the α-phase absorbs strongly at 530 cm^{-1}, 615 cm^{-1}, 765-766 cm^{-1} and 795 cm^{-1}, the absorption values for the β- and γ- phases coincide at 510 cm^{-1} and 840 cm^{-1} with distinct γ-phase values of 431 cm^{-1}, 776 cm^{-1}, 812 cm^{-1}, 833 cm^{-1}, and 1233 cm^{-1} [44]. This overlap arises from the presence of the vibrational modes along the orthorhombic unit cell axes in the PVDF crystal.

The PVDF β-phase unit cell has lattice parameters $a = 8.58$Å, $b = 4.91$Å, and $c = 2.56$Å [9,31,85]. The expression for the vibrational species predicts five A_1 bands with polarization parallel to the b unit cell parameter axis, three B_1 bands with polarization parallel to the the c unit cell axis and four B_1 bands with polarization parallel to the unit cell a axis. However, the unit cells for the α-phase and γ-phase are also orthorhombic with parameters varying by only a few Å [9, 31, 85]. When the potential lattice distortion arising from the presence of the copolymer is considered, the difficulty distinguishing between the various phases increases.

Benz et al. address many of the issues using FTIR alone to resolve the different phases, and provide the following relations to determine crystallinity from IR data:

$$A_{762} = {K_\alpha}^{762} X_\alpha t$$

$$A_{1275} = {K_\beta}^{1275} X_\beta t$$

$$A_{835} = ({K_\beta}^{835} X_\beta + {K_\gamma}^{835} X_\gamma + {K_{am}}^{835}(1 - X_{total}))t$$

with A_j the baseline-corrected absorbance at j cm^{-1}, $K_i{}^j$ the absorption coefficient at j cm^{-1} for the i^{th} phase, X_i the mole fraction of the i^{th} phase, X_{total} the total crystallinity of the sample, and t the thickness in µm [44].

If a thin film is known to contain only two of the three electroactive phases (i.e. α-β, β-γor α-γstructures only), then Gregorio's equation

$$F(\beta) = \frac{X_\beta}{X_\alpha + X_\beta} = \frac{A_\beta}{(K_\beta/K_\alpha)A_\alpha + A_\beta}$$

with X_α and X_β representing the mass fraction of the α-phase and β-phase, A_α and A_β representing absorption bands at 763 cm^{-1} and 840 cm^{-1} respectively, and K_α and K_β representing the respective wavenumber [9, 32].

Even with the above equations, the overlap of peaks should be addressed through deconvolution [9]. Further issues arise given any variability in copolymer percentage in a PVDF-copolymer thin film.

Differential Scanning Calorimetry

Differential scanning calorimetry (DSC) is thermoanalytic technique comparing the amount of heat required to change the temperature of a test sample to a the amount of heat required to change the temperature of a known reference.

Benz et al. report the enthalpy of fusion for β-phase PVDF as $\Delta H_\infty = 104.6$ J/g [44], and the α-, β-, and γ-phases of PVDF melting at 167 °C to 172 °C [9, 44] with Martins et al. reporting a range of 179 °C to 180 °C for the γ-phase [32]. The melting temperature includes a dependence on thin film fabrication method, crysolite size, and the presence of defects, ; these paramters prevent experimenters from identifying a specific phase with a given temperature [32]. However, when used in conjunction with other analytical techniques, DSC can provide valuable insight into the film structure and phase content.

4. CONCLUSION

Creating high-content β-phase PVDF-HFP thin films continues to be as much an art as a science. This is partly due to the possibilities inherent to the nature of the PVDF molecule, its many orientations and the available transitions between phases. However, the susceptibility of a PVDF thin film to an every-varying list of laboratory parameters seems to interfere with establishing a concrete path to its most desired qualities. In short, when creating a PVDF thin film the fabrication approach dominates the final thin film behavior–from crystal phase to melting point, even though the melting point is not dependent on the crystal phase.

Controlling the laboratory environment then becomes the priority. Langmuir-Blodgett is only a superficially simple method of fabricating thin film structures. In Section 2.1, the physics motivating why precise control over the dipping angle in the Langmuir-Blodgett fabrication approach is of utmost importance, along with control over the surface pressure and dipping rate. During the dipping process there are many interacting parameters affecting the formation of the thin film, and no clear path to tie a particular parameter to a final property in the thin film using characterization methods currently available. For example, experimental results show that the choice of solvent has an immediate and direct impact on the quality of the thin film [70], but researchers are not only left to ambiguously decide which solvent is appropriate for a given application, but also how to predict the ways a solvent will affect the thin film formation. The physical LB model alone is not sufficient to answer these questions.

In an attempt to gain control over some of these parameters, customized equipment was created to enable repeatable, automated sample fabrication. Samples fabricated with this equipment were then characterized using ferroelectric hysteresis measurements, AFM, and SEM. Not only did these characterization results show remarkable improvement in fabricated device quality over previous methods, the de-

velopment of a software-based approach to ferroelectric hysteresis measurements removes hardware dependence and constraints. This obviates the need for filters and corrections during data analysis, and eases the data collection process.

The automated Langmuir-Blodgett deposition system will continue to be improved through the construction of a pressurized environment for the Langmuir-Blodgett Trough. This environment will be filled with an inert gas (e.g. Nitrogen) and the inert environment will help prevent the formation of oxygen vacancies during thin film fabrication, leading to a reduction in ferroelectric fatigue [12]. Additional immediate improvement is achievable by implementing microstepping with the LB trough dipping mechanism's stepper motor, reducing system vibration and allowing for more dipping rates.

The current LabVIEW implementation of the two-pulse hysteresis measurement can be greatly optimized by better parameter calculations during the first stage of the program, eliminating the need for multiple calls to the Keithley subVI during the main for-loop. This will allow the program to operate with more efficiency, and enable better sampling rates and data collection.

Finally, much of the fundamental work characterizing PVDF is in need of repeating for PVDF with its copolymers. The physical theory is well established, but the constants required to practically implement the material in devices are frequently lacking. Successfully determining these constant parameters could easily lead to a large gain in polymer science for the cost of some easily repeated work.

The various thin film analysis methods presented in Section 3.2 provide limited insight into how the parameters such as dipping speed and dipping angle interact during the deposition process. However, even if all of the connections between fabrication parameters and thin film characteristics are made, the optimization problem remains. How do we achieve the desired result of PVDF thin films with high electric coercivity most efficiently?

Combining the large and ongoing collection of data scrutinizing PVDF with the more sparse information concerning its copolymers could provide the foundations

for a "big data" set suitable for machine learning analysis. Computational methods already exist for optimizing experimental approaches [86, 87], and material science applications of machine learning algorithms continue to be developed [88–91].

Together, machine learning and optimization of experiment design provide a path for more efficient experimentation where one physical/machine learning model is developed for the experiment and another physical/machine learning analyzes the data gathered by the experiment. By using this combined approach, it may be possible to use data collected for PVDF thus far and implement transfer learning to adjust for various copolymer structures.

REFERENCES

[1] Egon Barth. Materials for pipes - meeting changing requirements. *100 Years of Kunstoffe*, pages 6–11, 2010.

[2] Arkema. *Kynar & Kynar Flex PVDF Performance Characteristics and Data - Thermoplastics for Engineering Applications*, 10 2009.

[3] Jeffrey Carvell and Ruihua Cheng. Study of electrical polarization hysteresis in ferroelectric polyvinylidene fluoride films. *Materials Letters*, 64(18):1992–1995, 2010.

[4] Huie Zhu, Masaya Mitsuishi, and Tokuji Miyashita. Facile preparation of highly oriented poly (vinylidene fluoride) langmuir–blodgett nanofilms assisted by amphiphilic polymer nanosheets. *Macromolecules*, 45(22):9076–9084, 2012.

[5] Hemalatha Parangusan, Deepalekshmi Ponnamma, and Mariam Al Ali Al-Maadeed. Stretchable electrospun pvdf-hfp/co-zno nanofibers as piezoelectric nanogenerators. *Scientific reports*, 8(1):754, 2018.

[6] Zhihua Ying, Yadong Jiang, Xiaosong Du, Guangzhong Xie, and Yajie Yang. A study of pvdf langmuir-blodgett thin film using quartz crystal microbalance. *Journal of applied polymer science*, 106(2):1024–1027, 2007.

[7] John S Dodds, Frederick N Meyers, and Kenneth J Loh. Piezoelectric characterization of pvdf-trfe thin films enhanced with zno nanoparticles. *IEEE Sensors Journal*, 12(6):1889–1890, 2011.

[8] Mengjun Bai, AV Sorokin, Daniel W Thompson, Matt Poulsen, Stephen Ducharme, CM Herzinger, S Palto, VM Fridkin, SG Yudin, VE Savchenko, et al. Determination of the optical dispersion in ferroelectric vinylidene fluoride (70%)/trifluoroethylene (30%) copolymer langmuir–blodgett films. *Journal of applied physics*, 95(7):3372–3377, 2004.

[9] Liuxia Ruan, Xiannian Yao, Yufang Chang, Lianqun Zhou, Gaowu Qin, and Xianmin Zhang. Properties and applications of the β phase poly (vinylidene fluoride). *Polymers*, 10(3):228, 2018.

[10] G Hao, A Mosey, X Jiang, AJ Yost, KR Sapkota, GT Wang, X Zhang, Jian Zhang, AT N'Diaye, R Cheng, et al. Nonvolatile voltage controlled molecular spin state switching. *Applied Physics Letters*, 114(3):032901, 2019.

[11] Andrew J Lovinger. Ferroelectric polymers. *Science*, 220(4602):1115–1121, 1983.

[12] Alexander K Tagantsev, I Stolichnov, EL Colla, and N Setter. Polarization fatigue in ferroelectric films: Basic experimental findings, phenomenological scenarios, and microscopic features. *Journal of Applied Physics*, 90(3):1387–1402, 2001.

[13] João Gomes, J Serrado Nunes, Vitor Sencadas, and Senentxu Lanceros-Méndez. Influence of the β-phase content and degree of crystallinity on the piezo-and ferroelectric properties of poly (vinylidene fluoride). *Smart Materials and Structures*, 19(6):065010, 2010.

[14] Gene H Haertling. Ferroelectric ceramics: history and technology. *Journal of the American Ceramic Society*, 82(4):797–818, 1999.

[15] Jacques Curie and Pierre Curie. Development by pressure of polar electricity in hemihedral crystals with inclined faces. *Bull. soc. min. de France*, 3:90, 1880.

[16] Jeffrey S Cross, Mitsushi Fujiki, Mineharu Tsukada, Yasutoshi Kotaka, and Yasuyuki Goto. Characterization of pzt capacitors with srruo3 electrodes. *Integrated Ferroelectrics*, 21(1-4):263–271, 1998.

[17] L. E. Cross and R. E. Newnham. History of ferroelectrics. *Ceramics and Civilization*, 3, 1987.

[18] Joseph Valasek. Piezo-electric and allied phenomena in rochelle salt. *Physical review*, 17(4):475, 1921.

[19] H Kliem and R Tadros-Morgane. Extrinsic versus intrinsic ferroelectric switching: experimental investigations using ultra-thin pvdf langmuir–blodgett films. *Journal of Physics D: Applied Physics*, 38(12):1860, 2005.

[20] RCG Naber, PWM Blom, and DM De Leeuw. Comment on 'extrinsic versus intrinsic ferroelectric switching: experimental investigations using ultra-thin pvdf langmuir–blodgett films'. *Journal of Physics D: Applied Physics*, 39(9):1984, 2006.

[21] Matthew Poulsen and Stephen Ducharme. Why ferroelectric polyvinylidene fluoride is special. *IEEE Transactions on Dielectrics and Electrical Insulation*, 17(4):1028–1035, 2010.

[22] Walter J Merz. Domain formation and domain wall motions in ferroelectric bati o 3 single crystals. *Physical Review*, 95(3):690, 1954.

[23] Ennio Fatuzzo and Walter J Merz. Switching mechanism in triglycine sulfate and other ferroelectrics. *Physical Review*, 116(1):61, 1959.

[24] Ennio Fatuzzo. Theoretical considerations on the switching transient in ferroelectrics. *Physical review*, 127(6):1999, 1962.

[25] BB Tian, LF Chen, Yi Liu, XF Bai, JL Wang, Sh Sun, GL Yuan, JL Sun, B Dkhil, XJ Meng, et al. Homogeneous switching mechanism in pure polyvinylidene fluoride ultrathin films. *Physical Review B*, 92(6):060102, 2015.

[26] Shi Liu, Ilya Grinberg, and Andrew M Rappe. Intrinsic ferroelectric switching from first principles. *Nature*, 534(7607):360, 2016.

[27] Yingfen Wei, Pavan Nukala, Mart Salverda, Sylvia Matzen, Hong Jian Zhao, Jamo Momand, Arnoud S Everhardt, Guillaume Agnus, Graeme R Blake, Philippe Lecoeur, et al. A rhombohedral ferroelectric phase in epitaxially strained hf 0.5 zr 0.5 o 2 thin films. *Nature Materials*, 17(12):1095, 2018.

[28] Stephen Ducharme, Timothy J Reece, Christina M Othon, and Randy K Rannow. Ferroelectric polymer langmuir-blodgett films for nonvolatile memory applications. *IEEE Transactions on Device and Materials Reliability*, 5(4):720–735, 2005.

[29] H Kawai. The piezoelectricity of pvdf japan j. *Appl. Phys*, 8:975, 1969.

[30] Stephen Ducharme. Why are ferroelectric polymers difficult to find—and difficult to verify. In *2008 13th International Symposium on Electrets*, pages B0501–B0501. IEEE, 2008.

[31] Kohji Tashiro. Crystal structure and phase transition of pvdf and related copolymers. *Ferroelectric Polymers: Chemistry Physics and Applications*, 28:63–182, 1995.

[32] P Martins, AC Lopes, and S Lanceros-Mendez. Electroactive phases of poly (vinylidene fluoride): Determination, processing and applications. *Progress in polymer science*, 39(4):683–706, 2014.

[33] Francesco Pelizza and Karen Johnston. A density functional theory study of poly (vinylidene difluoride) crystalline phases. *Polymer*, page 121585, 2019.

[34] David B Hall, Patrick Underhill, and John M Torkelson. Spin coating of thin and ultrathin polymer films. *Polymer Engineering & Science*, 38(12):2039–2045, 1998.

[35] C Alemany, R Jimenez, J Revilla, J Mendiola, and ML Calzada. Pulsed hysteresis loops on ferroelectric thin films. *Journal of Physics D: Applied Physics*, 32(17):L79, 1999.

[36] T. Furukawa, M. Date, and E. Fukada. Hysteresis phenomena in polyvinylidene fluoride under high electric field. *Journal of Applied Physics*, 51(2):1135–1141, 1980.

[37] Michael Wegener. Polarization-electric field hysteresis of ferroelectric pvdf films: Comparison of different measurement regimes. *Review of Scientific Instruments*, 79(10):106103, 2008.

[38] Xujiang He, Kui Yao, and Bee Keen Gan. Ferroelectric poly (vinylidene fluoride-hexafluoropropylene) thin films on silicon substrates. *Sensors and Actuators A: Physical*, 139(1-2):158–161, 2007.

[39] Ambalangodage C Jayasuriya, Adriana Schirokauer, and Jerry I Scheinbeim. Crystal-structure dependence of electroactive properties in differently prepared poly (vinylidene fluoride/hexafluoropropylene) copolymer films. *Journal of Polymer Science Part B: Polymer Physics*, 39(22):2793–2799, 2001.

[40] Mengjun Bai. *The structure of ferroelectric PVDF/TrFE copolymer Langmuir–Blodgett films*. PhD thesis, Ph. D. thesis, Dept. Physics and Astronomy, Univ. Nebraska, Lincoln, 2002.

[41] Ying Hou, Zhaoyue Lü, Tiansong Pu, Yuan Zhang, Xiangjian Meng, and Haisheng Xu. Unipolar poling-induced high switching speed and improved imprint behaviors for poly (vinylidene fluoride-trifluoroethylene) copolymer ultrathin films. *Applied Physics Letters*, 103(26):263503, 2013.

[42] Yoshiro Tajitsu, Ayumu Hirooka, Akira Yamagish, and Munehiro Date. Ferroelectric behavior of thin films of vinylidene fluoride/trifluoroethylene/hexafluoropropylene copolymer. *Japanese journal of applied physics*, 36(9S):6114, 1997.

[43] Xujiang He, Kui Yao, and Bee Keen Gan. Phase transition and properties of a ferroelectric poly (vinylidene fluoride-hexafluoropropylene) copolymer. *Journal of applied physics*, 97(8):084101, 2005.

[44] Marcel Benz and William B Euler. Determination of the crystalline phases of poly (vinylidene fluoride) under different preparation conditions using differential scanning calorimetry and infrared spectroscopy. *Journal of applied polymer science*, 89(4):1093–1100, 2003.

[45] Abraham Ulman. *An Introduction to Ultrathin Organic Films: From Langmuir–Blodgett to Self–Assembly*. Academic press, 2013.

[46] SD Bernstein, TY Wong, Yanina Kisler, and RW Tustison. Fatigue of ferroelectric pbzr x ti y o 3 capacitors with ru and ruo x electrodes. *Journal of materials research*, 8(1):12–13, 1993.

[47] Orlando Auciello, Kenneth D Gifford, Daniel J Lichtenwalner, Rovindra Dat, Husam N Al-Shareef, Kashyap R Bellur, and Angus I Kincon. A review of composition-structure-property relationships for pzt-based heterostructure capacitors. *Integrated Ferroelectrics*, 6(1-4):173–187, 1995.

[48] Nobuhiko P Kobayashi, Carrie L Donley, Shih-Yuan Wang, and R Stanley Williams. Atomic layer deposition of aluminum oxide on hydrophobic and hydrophilic surfaces. *Journal of Crystal Growth*, 299(1):218–222, 2007.

[49] JC Fisher and Ivar Giaever. Tunneling through thin insulating layers. *Journal of Applied Physics*, 32(2):172–177, 1961.

[50] AJA International. A300 series, a3cv & ctm magnetron sputtering sources installation & operation manual, December 2004.

[51] Peter J Kelly and R Derek Arnell. Magnetron sputtering: a review of recent developments and applications. *Vacuum*, 56(3):159–172, 2000.

[52] RV Stuart and GK Wehner. Energy distribution of sputtered cu atoms. *Journal of Applied Physics*, 35(6):1819–1824, 1964.

[53] GK Wehner. Velocities of sputtered atoms. *Physical Review*, 114(5):1270, 1959.

[54] Edgar Alfonso, Jairo Olaya, and Gloria Cubillos. Thin film growth through sputtering technique and its applications. *Crystallization–Science and Technology*, pages 397–432, 2012.

[55] B Window and N Savvides. Unbalanced dc magnetrons as sources of high ion fluxes. *Journal of Vacuum Science & Technology A: Vacuum, Surfaces, and Films*, 4(3):453–456, 1986.

[56] Agnes Pockels. Relations between the surface-tension and relative contamination of water surfaces, 1893.

[57] Irving Langmuir. Pilgrim trust lecture, molecular layers. *Proceedings of the Royal Society of London. Series A. Mathematical and Physical Sciences*, 170(940):1–39, 1939.

[58] Katharine B. Blodgett and Irving Langmuir. Built-up films of barium stearate and their optical properties. *Phys. Rev.*, 51:964–982, Jun 1937.

[59] MJ Grundy, RJ Musgrove, RM Richardson, SJ Roser, and J Penfold. Effect of dipping rate on alternating layer langmuir-blodgett film structure. *Langmuir*, 6(2):519–521, 1990.

[60] JE Riegler. Fluorescence microscope for real-time studies of langmuir–blodgett layer deposition. *Review of scientific instruments*, 59(10):2220–2224, 1988.

[61] JE Riegler and JD LeGrange. Observation of a monolayer phase transition on the meniscus in a langmuir-blodgett transfer configuration. *Physical review letters*, 61(21):2492, 1988.

[62] Pierre-Gilles de Gennes. Deposition of langmuir-blodgett layers. *Colloid and Polymer Science*, 264(5):463–465, 1986.

[63] MR Buhaenko and RM Richardson. Measurements of the forces of emersion and immersion and contact angles during langmuir-blodgett deposition. *Thin Solid Films*, 159(1-2):231–238, 1988.

[64] Syun Egusa, Nobuhiro Gemma, and Makoto Azuma. Experimental analysis of the thermodynamic mechanism of langmuir-blodgett film transfer. *Journal of Physical Chemistry*, 94(6):2512–2518, 1990.

[65] TD Blake and JM Haynes. Kinetics of liquidliquid displacement. *Journal of colloid and interface science*, 30(3):421–423, 1969.

[66] Peter G. Petrov. Dynamics of deposition of langmuir–blodgett multilayers. *J. Chem. Soc., Faraday Trans.*, 93:295–302, 1997.

[67] J Mahnke, D Vollhardt, KW Stöckelhuber, K Meine, and HJ Schulze. Regular stripe patterns in skeletonized langmuir- blodgett films of arachidic acid. *Langmuir*, 15(23):8220–8224, 1999.

[68] KSV. Ksv minitrough instruction manual, 1991.

[69] DuPont. *DuPont Delrin Acetal Homopolymer White Paper: How to Maximize the Property Advantages of Delrin Acetal Homopolymer over Acetal Copolymer - A Guide for Design Engineers*. DuPont, 2015.

[70] Huie Zhu, Jun Matsui, Shunsuke Yamamoto, Tokuji Miyashita, and Masaya Mitsuishi. Solvent-dependent properties of poly (vinylidene fluoride) monolayers at the air–water interface. *Soft Matter*, 11(10):1962–1972, 2015.

[71] Brian J Rodriguez, Stephen Jesse, Sergei V Kalinin, Jihee Kim, Stephen Ducharme, and VM Fridkin. Nanoscale polarization manipulation and imaging of ferroelectric langmuir-blodgett polymer films. *Applied physics letters*, 90(12):122904, 2007.

[72] K Pramod, Binaya Kumar Sahu, and RB Gangineni. Resistance switching in polyvinylidene fluoride (pvdf) thin films. In *AIP Conference Proceedings*, volume 1665, page 110051. AIP Publishing, 2015.

[73] Xujiang He and Kui Yao. Crystallization mechanism and piezoelectric properties of solution-derived ferroelectric poly (vinylidene fluoride) thin films. *Applied physics letters*, 89(11):112909, 2006.

[74] Marcel Benz, William B Euler, and Otto J Gregory. The role of solution phase water on the deposition of thin films of poly (vinylidene fluoride). *Macromolecules*, 35(7):2682–2688, 2002.

[75] Le Wang, Xiaoli Wang, and Jing Shi. Measurement and estimation of ferroelectric hysteresis loops. *Ferroelectrics*, 411(1):86–92, 2010.

[76] C. B. Sawyer and C. H. Tower. Rochelle salt as a dielectric. *Phys. Rev.*, 35:269–273, Feb 1930.

[77] MGCM Stewart, MG Cain, and DA Hall. *Ferroelectric hysteresis measurement and analysis*. National Physical Laboratory Teddington, 1999.

[78] Takeshi Yoshimura and Norifumi Fujimura. Polarization hysteresis loops of ferroelectric gate capacitors measured by sawyer-tower circuit. *Japanese journal of applied physics*, 42(9S):6011, 2003.

[79] Xunlin Qiu, Lars Holländer, Werner Wirges, Reimund Gerhard, and Heitor Cury Basso. Direct hysteresis measurements on ferroelectret films by means of a modified sawyer–tower circuit. *Journal of Applied Physics*, 113(22):224106, 2013.

[80] Susumu Ikeda, Shin'ichi Kobayashi, and Yasaku Wada. Analysis of the effect of electrical conductance of ferroelectric polymers on d-e hysteresis curves measured by the sawyer–tower method. *Journal of Polymer Science: Polymer Physics Edition*, 23(8):1513–1521, 1985.

[81] Peter Kis, Miklós Kuczmann, János Füzi, and Amalia Ivanyi. Hysteresis measurement in labview. *Physica B: Condensed Matter*, 343(1-4):357–363, 2004.

[82] Dragan Damjanovic. Hysteresis in piezoelectric and ferroelectric materials. *The science of hysteresis*, 3:337–465, 2006.

[83] Keithley. *Model 6487 Picoammeter/Voltage Source Reference Manual*, 3 2011.

[84] Peter A Dowben, Luis G Rosa, Carolina C Ilie, and Jie Xiao. Adsorbate/absorbate interactions with organic ferroelectric polymers. *Journal of Electron Spectroscopy and Related Phenomena*, 174(1-3):10–21, 2009.

[85] Ryozo Hasegawa, Masamichi Kobayashi, and Hiroyuki Tadokoro. Molecular conformation and packing of poly (vinylidene fluoride). stability of three crystalline forms and the effect of high pressure. *Polymer Journal*, 3(5):591, 1972.

[86] Krishna Rajan. *Informatics for materials science and engineering: data-driven discovery for accelerated experimentation and application*. Butterworth-Heinemann, 2013.

[87] Ankit Agrawal and Alok Choudhary. Perspective: Materials informatics and big data: Realization of the "fourth paradigm" of science in materials science. *Apl Materials*, 4(5):053208, 2016.

[88] Tim Mueller, Aaron Gilad Kusne, and Rampi Ramprasad. Machine learning in materials science: Recent progress and emerging applications. *Reviews in Computational Chemistry*, 29:186–273, 2016.

[89] Arun Mannodi-Kanakkithodi, Ghanshyam Pilania, Tran Doan Huan, Turab Lookman, and Rampi Ramprasad. Machine learning strategy for accelerated design of polymer dielectrics. *Scientific reports*, 6:20952, 2016.

[90] Arun Mannodi-Kanakkithodi, Anand Chandrasekaran, Chiho Kim, Tran Doan Huan, Ghanshyam Pilania, Venkatesh Botu, and Rampi Ramprasad. Scoping the polymer genome: A roadmap for rational polymer dielectrics design and beyond. *Materials Today*, 21(7):785–796, 2018.

[91] Stephen Wu, Yukiko Kondo, Masa-aki Kakimoto, Bin Yang, Hironao Yamada, Isao Kuwajima, Guillaume Lambard, Kenta Hongo, Yibin Xu, Junichiro Shiomi, et al. Machine-learning-assisted discovery of polymers with high thermal conductivity using a molecular design algorithm. *npj Computational Materials*, 5(1):5, 2019.

A. Software

A.1 Python Code for Automated Dipper

```
#include <Wire.h>
#include <Adafruit_MotorShield.h>
#include <TextFinder.h>
#include <SoftwareSerial.h>

// Create the motor shield object with the default I2C address
Adafruit_MotorShield AFMS = Adafruit_MotorShield();

// Connect a stepper motor
Adafruit_StepperMotor *myMotor = AFMS.getStepper(200, 2);

TextFinder  finder(Serial);
// how many comma seperated fields we expect
const int NUMBER_OF_FIELDS = 3;

// array holding values for all the fields
int values[NUMBER_OF_FIELDS];

//initialize values; will update later as needed
int dir1 = FORWARD;
int dir2 = FORWARD;
int steps1 = 0;
int steps2 = 0;
```

```
int steps2a = 0;
int steps2b = 0;
int motorspeed = 0;
bool calibrate = 0;
SoftwareSerial mySerial(10,11);


void setup() {
    // set up Serial library at 9600 bps
    Serial.begin(9600);
    Serial.println("Stepper test!");

    mySerial.begin(9600);
    mySerial.println("Hello World");

    // create with the default frequency 1.6KHz
    AFMS.begin();

    // 10 rpm
    myMotor->setSpeed(10);
}

void loop() {

// the current field being received
int fieldIndex = 0;

while(fieldIndex < NUMBER_OF_FIELDS)
    values[fieldIndex++] = finder.getValue();

calibrate = values[0];
```

```
motorspeed = values[1];
steps2 = values[2];

cal_val += String(values[0]);
mo_val += String(values[1]);
st_val += String(values[2]);

if(values[2] < 0 )
    {
    dir2 = BACKWARD;
    steps2 = -1 * values[2];
    }
else
    {
    dir2 = FORWARD;
    steps2 = values[2];
    }

if(calibrate == 0)
{//Calibration mode
    myMotor->setSpeed(motorspeed);
    myMotor->step(steps2, dir2, SINGLE);
    myMotor->release();
}

if(calibrate == 1)
{ //For dipping mode
    steps2a = steps2;
    steps2b = steps2;
    myMotor->setSpeed(motorspeed);
    myMotor->step(steps2a, FORWARD, SINGLE);
```

```
    delay(10);
    myMotor->step(steps2b, BACKWARD, SINGLE);
    myMotor->release();
}
}
```

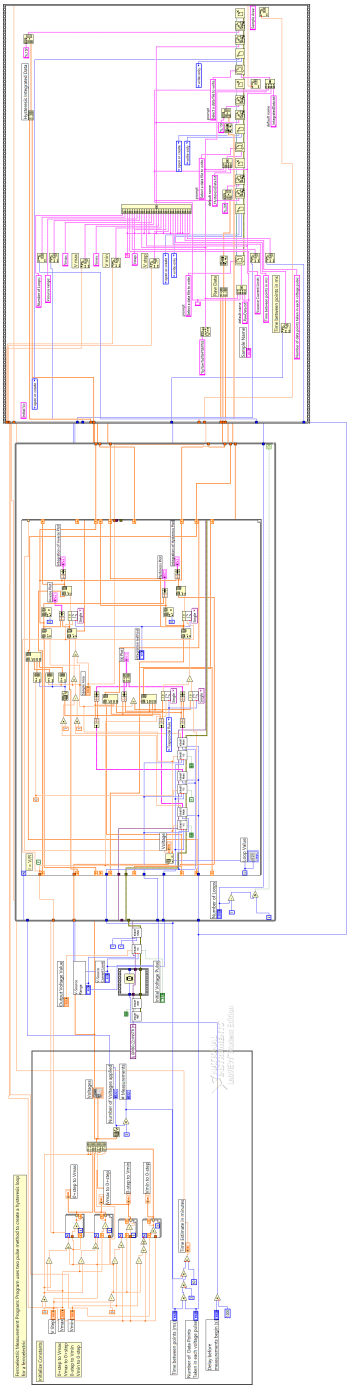

Figure A.1. LabVIEW Code for Ferroelectric Measurement.

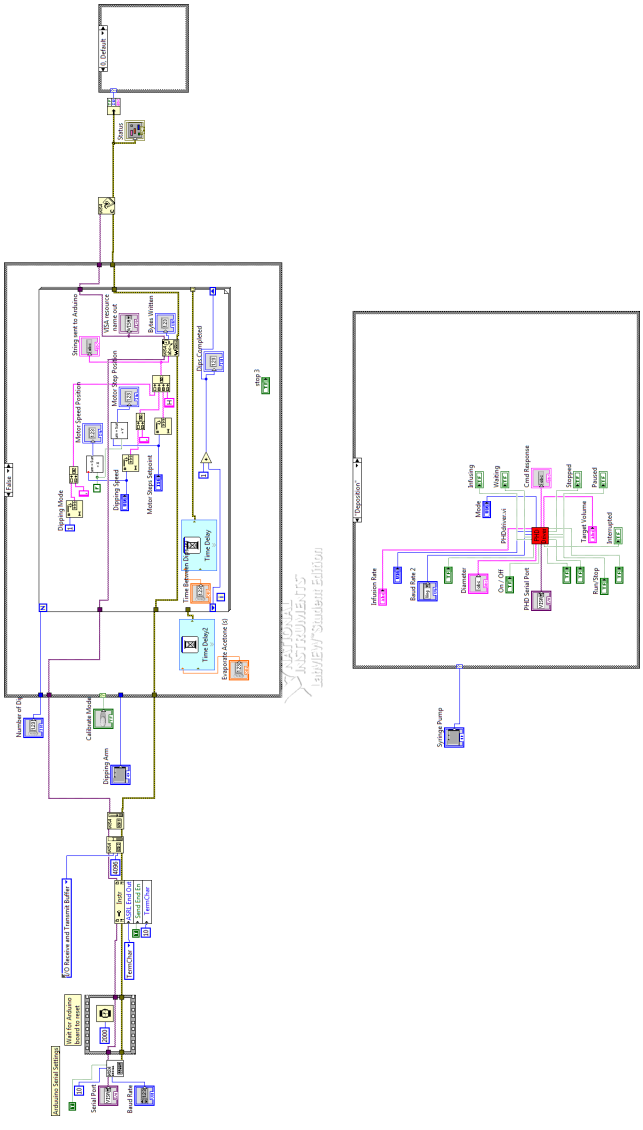

Figure A.2. LabVIEW Code for Arduino Uno Microcontroller and Syringe Pump.

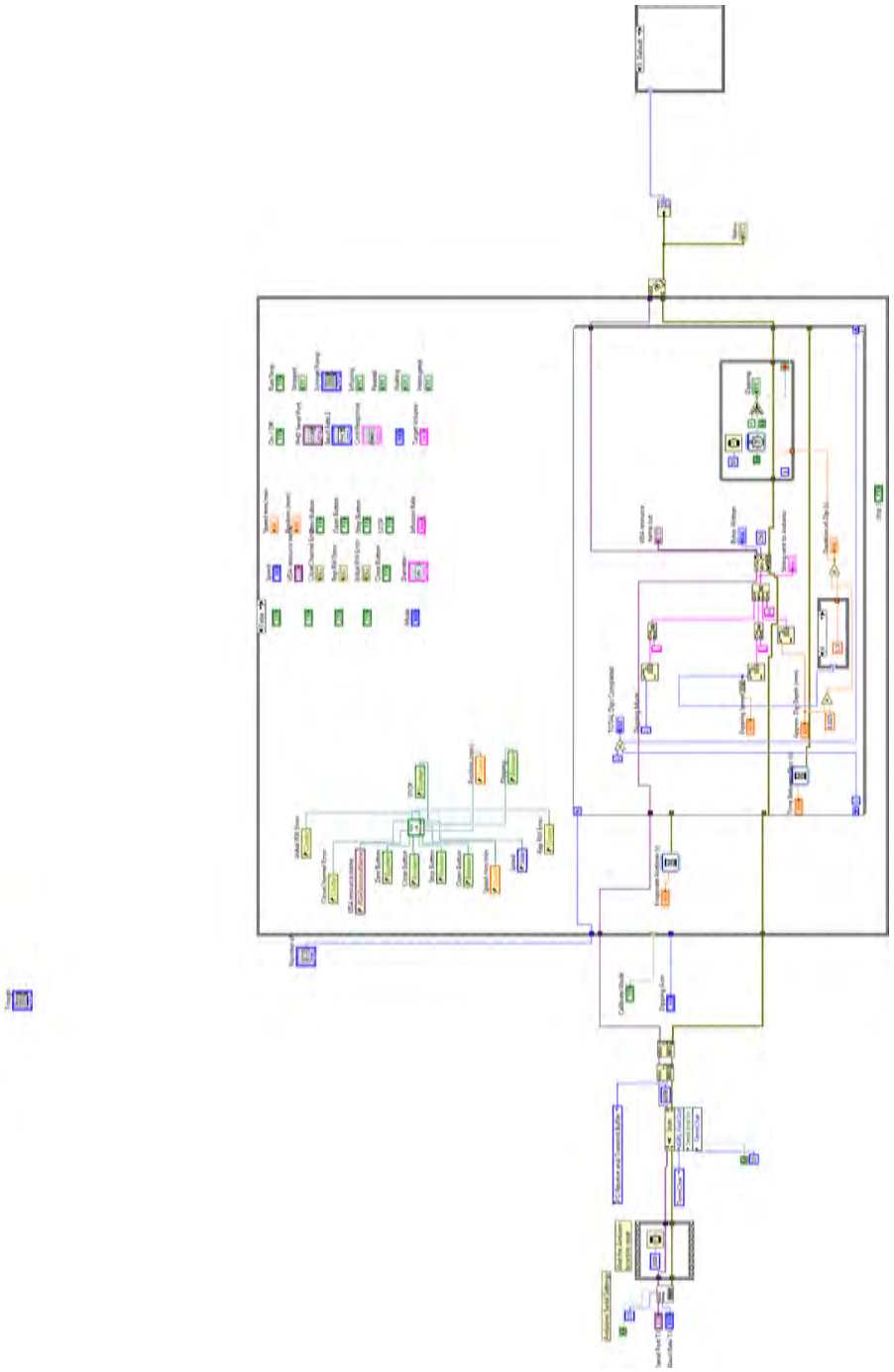

Figure A.3. LabVIEW Code for Automated LB Deposition System.

B. Calibration Data

B.1 Calibration of Tungsten-Alumina Wire Basket

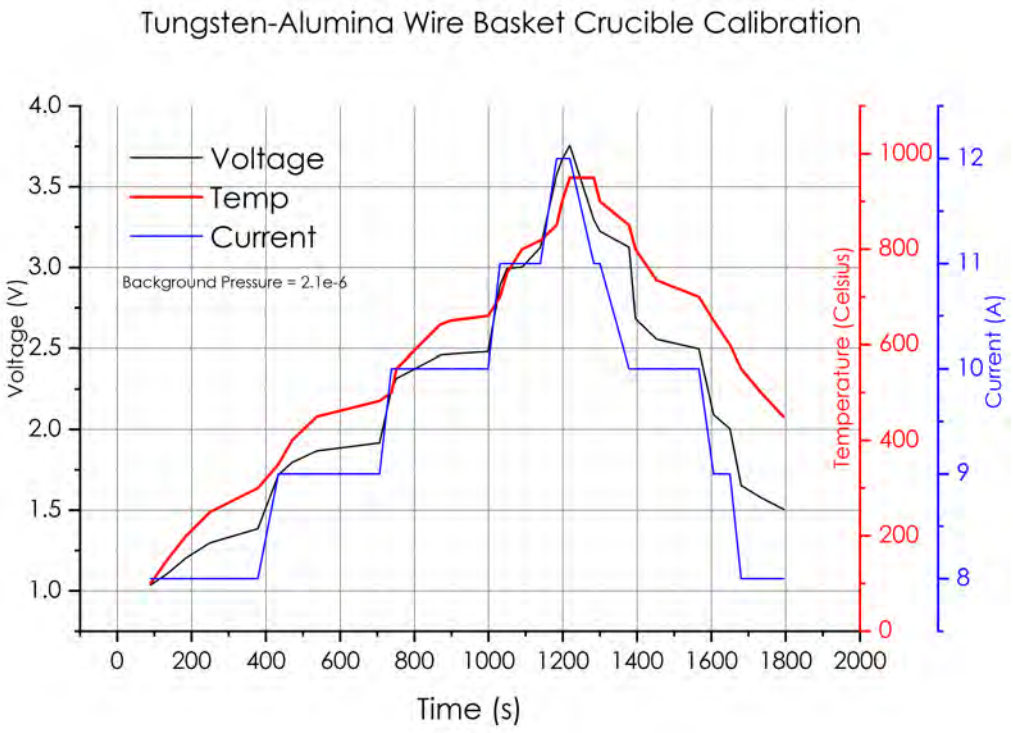

Figure B.1. Calibration data for tungsten-alumina wire basket crucible used in thermal evaporation.

C. Hardware Specifications

C.1 Stepper Motor for Adafruit Motor Shield

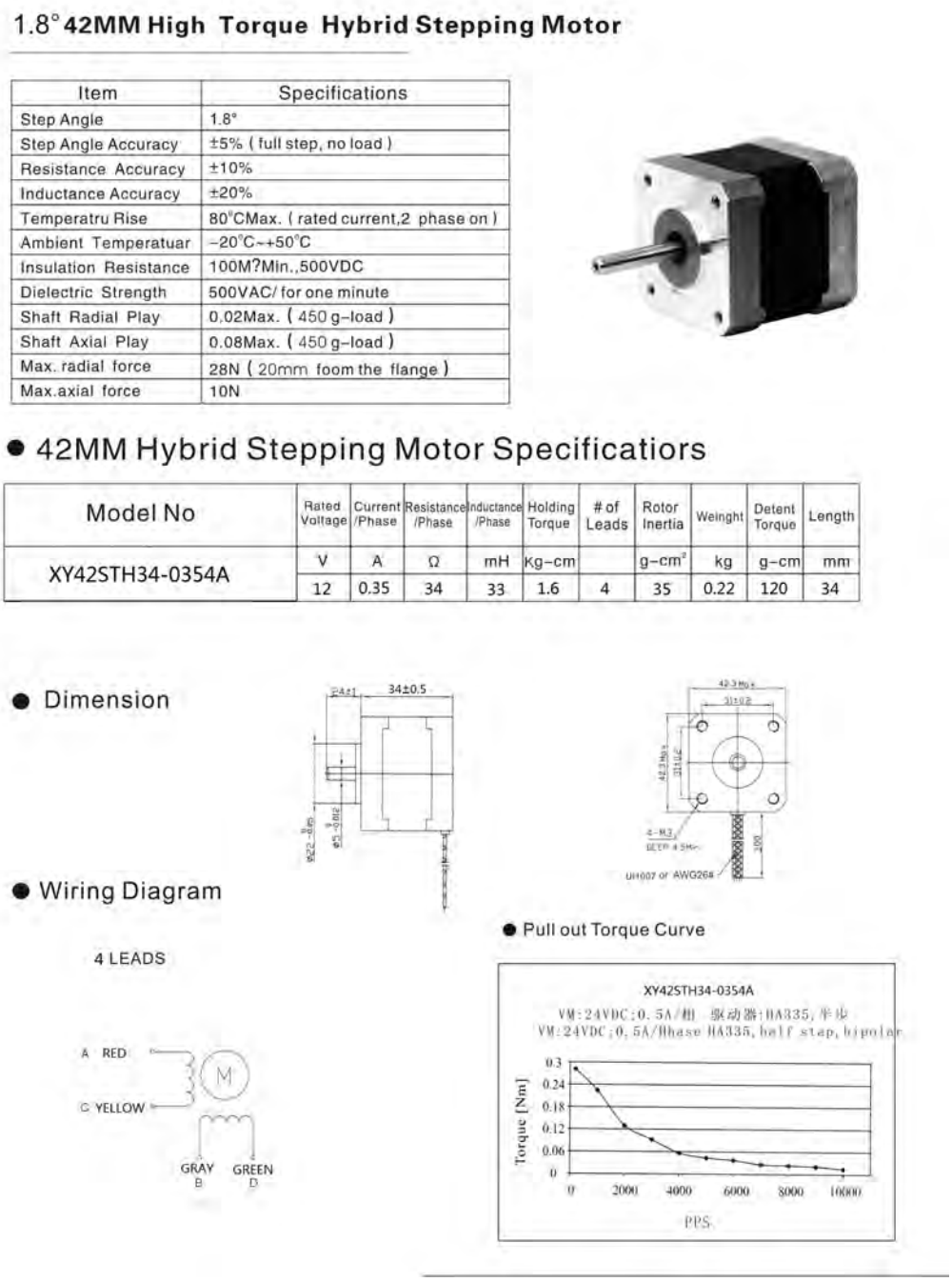

1.8° 42MM High Torque Hybrid Stepping Motor

Item	Specifications
Step Angle	1.8°
Step Angle Accuracy	±5% (full step, no load)
Resistance Accuracy	±10%
Inductance Accuracy	±20%
Temperatru Rise	80°CMax. (rated current,2 phase on)
Ambient Temperatuar	-20°C~+50°C
Insulation Resistance	100M?Min.,500VDC
Dielectric Strength	500VAC/ for one minute
Shaft Radial Play	0.02Max. (450 g-load)
Shaft Axial Play	0.08Max. (450 g-load)
Max. radial force	28N (20mm foom the flange)
Max.axial force	10N

● 42MM Hybrid Stepping Motor Specificatiors

Model No	Rated Voltage	Current /Phase	Resistance /Phase	Inductance /Phase	Holding Torque	# of Leads	Rotor Inertia	Weinght	Detent Torque	Length
XY42STH34-0354A	V	A	Ω	mH	Kg-cm		g-cm²	kg	g-cm	mm
	12	0.35	34	33	1.6	4	35	0.22	120	34

● Dimension

● Wiring Diagram

4 LEADS

A RED
C YELLOW
GRAY B
GREEN D

● Pull out Torque Curve

XY42STH34-0354A

VM:24VDC;0.5A/相 驱动器:HA335,半步

VM:24VDC;0.5A/Hhase HA335,half step,bipolar

Torque [Nm]

0.3 0.24 0.18 0.12 0.06 0

0 2000 4000 6000 8000 10000

PPS

Figure C.1. Technical data sheet for NEMA-17 stepper motor used in LB trough dipping arm.

C.2 Adafruit Motor Shield IC Datasheet

Toshiba Bi-CD Integrated Circuit Silicon Monolithic

TB6612FNG

Driver IC for Dual DC motor

TB6612FNG is a driver IC for DC motor with output transistor in LD MOS structure with low ON-resistor. Two input signals, IN1 and IN2, can choose one of four modes such as CW, CCW, short brake, and stop mode.

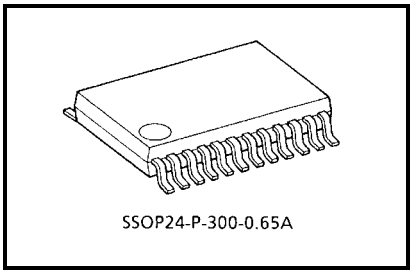

Weight: 0.14 g (typ.)

Features

- Power supply voltage: VM = 15 V(Max)
- Output current: I_{OUT} = 1.2 A(ave)/3.2 A (peak)
- Output low ON resistor: 0.5Ω (upper+lower Typ. @ VM ≥ 5 V)
- Standby (Power save) system
- CW/CCW/short brake/stop function modes
- Built-in thermal shutdown circuit and low voltage detecting circuit
- Small faced package(SSOP24: 0.65 mm Lead pitch)

* This product has a MOS structure and is sensitive to electrostatic discharge. When handling this product, ensure that the environment is protected against electrostatic discharge by using an earth strap, a conductive mat and an ionizer. Ensure also that the ambient temperature and relative humidity are maintained at reasonable levels.

Block Diagram

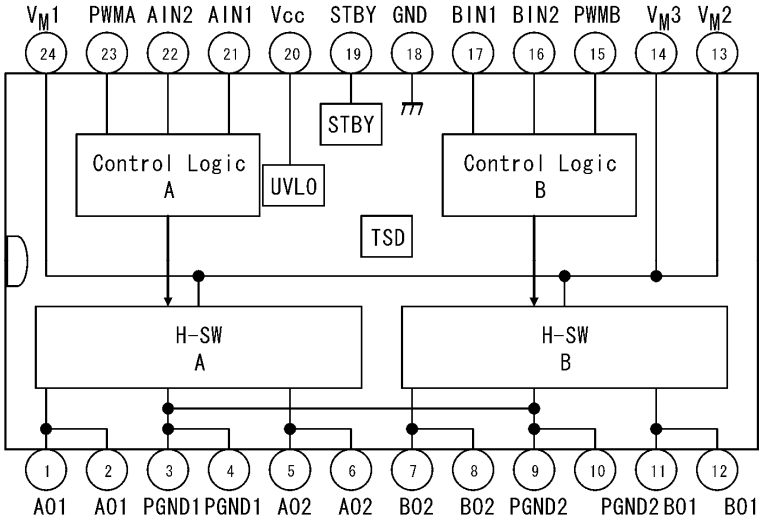

Pin Functions

No.	Pin Name	I/O	Function
1	AO1	O	ch A output 1
2	AO1		
3	PGND1	—	Power GND 1
4	PGND1		
5	AO2	O	ch A output 2
6	AO2		
7	BO2	O	ch B output 2
8	BO2		
9	PGND2	—	Power GND 2
10	PGND2		
11	BO1	O	ch B output 1
12	BO1		
13	VM2	—	Motor supply
14	VM3		
15	PWMB	I	ch B PWM input/200 kΩ pull-down at internal
16	BIN2	I	ch B input 2/200 kΩ pull-down at internal
17	BIN1	I	ch B input 1/200 kΩ pull-down at internal
18	GND	—	Small signal GND
19	STBY	I	“L” = standby/200 kΩ pull-down at internal
20	Vcc	—	Small signal supply
21	AIN1	I	ch A input 1/200 kΩ pull-down at internal
22	AIN2	I	ch A input 2/200 kΩ pull-down at internal
23	PWMA	I	ch A PWM input/200 kΩ pull-down at internal
24	VM1	—	Motor supply

Absolute Maximum Ratings (Ta = 25°C)

Characteristics	Symbol	Rating	Unit	Remarks
Supply voltage	VM	15	V	
	V_{CC}	6		
Input voltage	V_{IN}	-0.2 to 6	V	IN1,IN2,STBY,PWM pins
Output voltage	V_{OUT}	15	V	O1,O2 pins
Output current	I_{OUT}	1.2	A	Per 1 ch
	I_{OUT} (peak)	2		tw = 20 ms Continuous pulse, Duty ≤ 20%
		3.2		tw = 10 ms Single pulse
Power dissipation	P_D	0.78	W	IC only
		0.89		50 mm × 50 mm t = 1.6 mm Cu ≥ 40% in PCB mounting
		1.36		76.2 mm × 114.3 mm t = 1.6 mm Cu ≥ 30% in PCB monting
Operating temperature	T_{opr}	-20 to 85	°C	
Storage temperature	T_{stg}	-55 to 150	°C	

Operating Range (Ta = -20 to 85°C)

Characteristics	Symbol	Min	Typ.	Max	Unit	Remarks
Supply voltage	V_{CC}	2.7	3	5.5	V	
	VM	2.5	5	13.5	V	
Output current (H-SW)	I_{OUT}	—	—	1.0	A	VM ≥ 4.5 V
		—	—	0.4		4.5 V > VM ≥ 2.5 V Without PWM Operation
Switching frequency	f_{PWM}	—	—	100	kHz	

Input pin: IN1, IN2, PWM, STBY

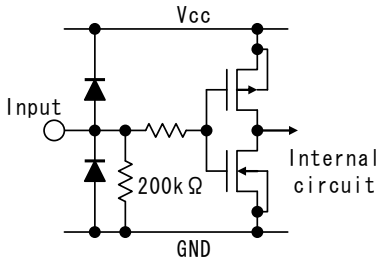

Output pin: O1, O2

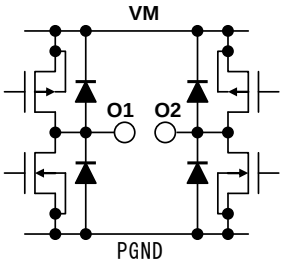

H-SW Control Function

Input				Output		
IN1	IN2	PWM	STBY	OUT1	OUT2	Mode
H	H	H/L	H	L	L	Short brake
L	H	H	H	L	H	CCW
		L	H	L	L	Short brake
H	L	H	H	H	L	CW
		L	H	L	L	Short brake
L	L	H	H	OFF (High impedance)		Stop
H/L	H/L	H/L	L	OFF (High impedance)		Standby

H-SW Operating Description

・To prevent penetrating current, dead time t2 and t4 is provided in switching to each mode in the IC.

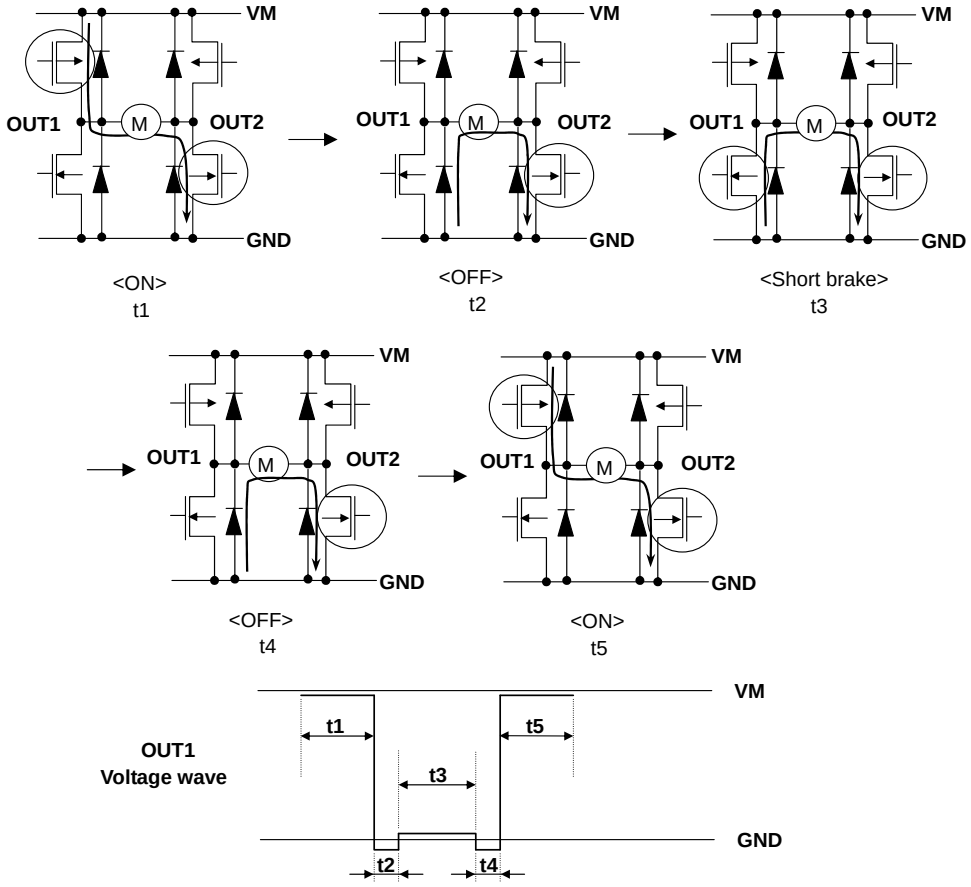

Electrical Characteristics (unless otherwise specified, Ta = 25°C, Vcc = 3 V, VM = 5 V)

Characteristics	Symbol		Test Condition	Min	Typ.	Max	Unit
Supply current	I_{CC}(3 V)		STBY = Vcc = 3 V, VM = 5 V	—	1.1	1.8	mA
	I_{CC}(5.5 V)		STBY = Vcc = 5.5 V, VM = 5 V	—	1.5	2.2	
	$I_{CC(STB)}$		STBY = 0 V	—	—	1	μA
	$I_{M(STB)}$			—	—	1	
Control input voltage	V_{IH}		—	Vcc×0.7	—	Vcc+0.2	V
	V_{IL}			-0.2	—	Vcc×0.3	
Control input current	I_{IH}		V_{IN} = 3 V	5	15	25	μA
	I_{IL}		V_{IN} = 0 V	—	—	1	
Standby input voltage	$V_{IH(STB)}$		—	Vcc×0.7	—	Vcc+0.2	V
	$V_{IL(STB)}$			-0.2	—	Vcc×0.3	
Standby input current	$I_{IH(STB)}$		V_{IN} = 3 V	5	15	25	μA
	$I_{IL(STB)}$		V_{IN} = 0 V	—	—	1	
Output saturating voltage	$V_{sat(U+L)1}$		I_O = 1 A, Vcc = VM = 5 V	—	0.5	0.7	V
	$V_{sat(U+L)2}$		I_O = 0.3 A, Vcc = VM = 5 V	—	0.15	0.21	
Output leakage current	$I_{L(U)}$		VM = V_{OUT} = 15 V	—	—	1	μA
	$I_{L(L)}$		VM = 15 V, V_{OUT} = 0 V	-1	—	—	
Regenerative diode VF	$V_{F(U)}$		I_F = 1A	—	1	1.1	V
	$V_{F(L)}$			—	1	1.1	
Low voltage detecting voltage	UVLD		(Design target only)	—	1.9	—	V
Recovering voltage	UVLC			—	2.2	—	
Response speed	t_r		(Design target only)	—	24	—	ns
	t_f			—	41	—	
	Dead time	H to L	Penetration protect time	—	50	—	
		L to H	(Design target only)	—	230	—	
Thermal shutdown circuit operating temperature	TSD		(Design target only)	—	175	—	°C
Thermal shutdown hysteresis	ΔTSD			—	20	—	

Target characteristics

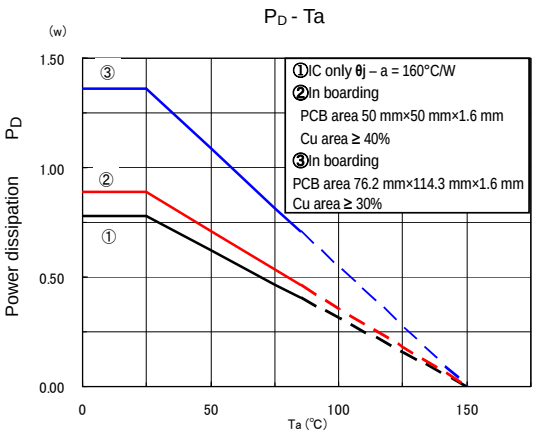

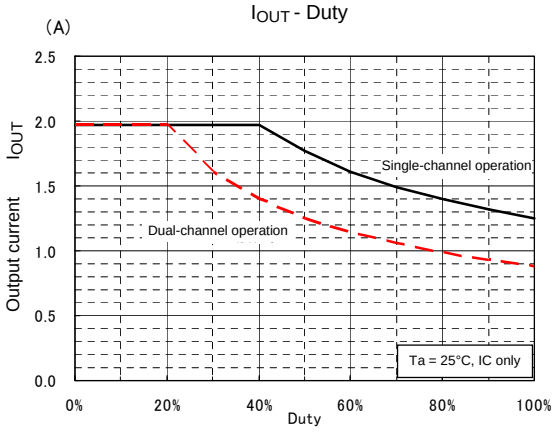

Typical Application Diagram

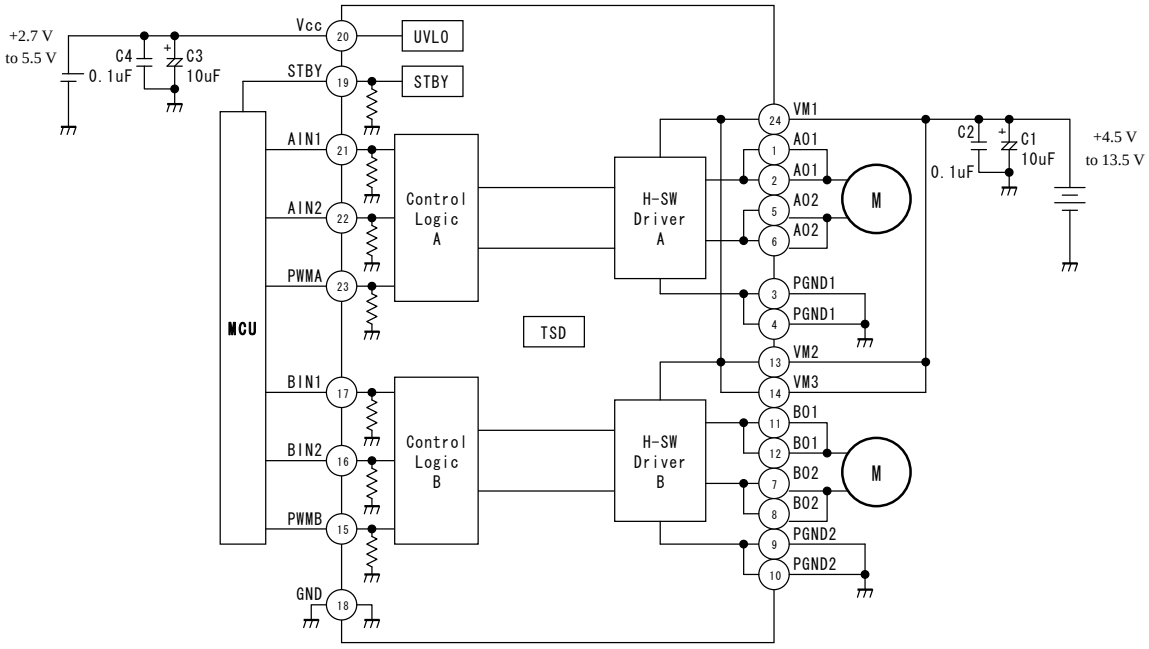

Note: Condensers for noise absorption (C1, C2, C3, and C4) should be connected as close as possible to the IC.

Package Dimennsions

SSOP24-P-300-0.65A "Unit : mm"

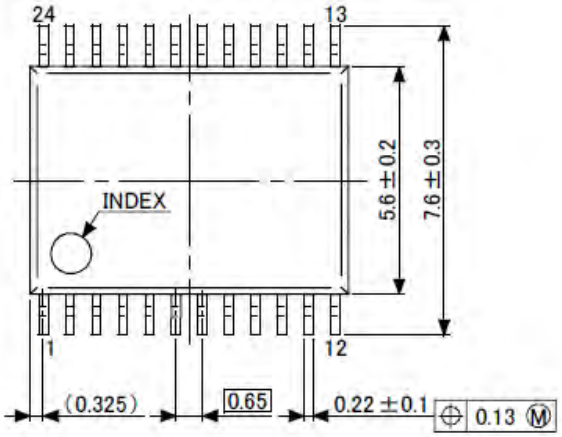

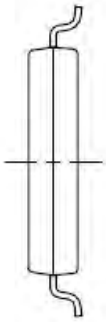

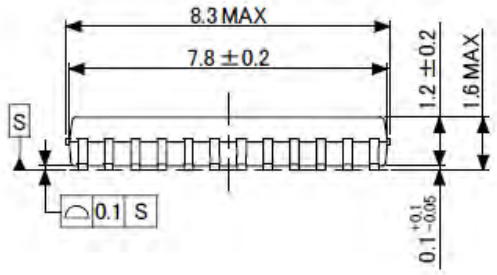

Detail of a terminal

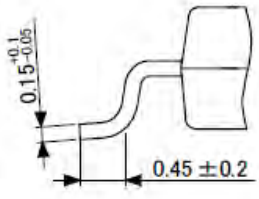

Weght: 0.14 g (typ)

Notes on Contents

1. Block Diagrams

Some of the functional blocks, circuits, or constants in the block diagram may be omitted or simplified for explanatory purposes.

2. Equivalent Circuits

The equivalent circuit diagrams may be simplified or some parts of them may be omitted for explanatory purposes.

3. Timing Charts

Timing charts may be simplified for explanatory purposes.

4. Application Circuits

The application circuits shown in this document are provided for reference purposes only. Thorough evaluation is required, especially at the mass production design stage.
Toshiba does not grant any license to any industrial property rights by providing these examples of application circuits.

5. Test Circuits

Components in the test circuits are used only to obtain and confirm the device characteristics. These components and circuits are not guaranteed to prevent malfunction or failure from occurring in the application equipment.

IC Usage Considerations

Notes on handling of ICs

[1] The absolute maximum ratings of a semiconductor device are a set of ratings that must not be exceeded, even for a moment. Do not exceed any of these ratings.
Exceeding the rating(s) may cause the device breakdown, damage or deterioration, and may result injury by explosion or combustion.

[2] Use an appropriate power supply fuse to ensure that a large current does not continuously flow in case of over current and/or IC failure. The IC will fully break down when used under conditions that exceed its absolute maximum ratings, when the wiring is routed improperly or when an abnormal pulse noise occurs from the wiring or load, causing a large current to continuously flow and the breakdown can lead smoke or ignition. To minimize the effects of the flow of a large current in case of breakdown, appropriate settings, such as fuse capacity, fusing time and insertion circuit location, are required.

[3] If your design includes an inductive load such as a motor coil, incorporate a protection circuit into the design to prevent device malfunction or breakdown caused by the current resulting from the inrush current at power ON or the negative current resulting from the back electromotive force at power OFF. IC breakdown may cause injury, smoke or ignition.
Use a stable power supply with ICs with built-in protection functions. If the power supply is unstable, the protection function may not operate, causing IC breakdown. IC breakdown may cause injury, smoke or ignition.

[4] Do not insert devices in the wrong orientation or incorrectly.
Make sure that the positive and negative terminals of power supplies are connected properly.
Otherwise, the current or power consumption may exceed the absolute maximum rating, and exceeding the rating(s) may cause the device breakdown, damage or deterioration, and may result injury by explosion or combustion.
In addition, do not use any device that is applied the current with inserting in the wrong orientation or incorrectly even just one time.

Points to remember on handling of ICs

(1) Thermal Shutdown Circuit

Thermal shutdown circuits do not necessarily protect ICs under all circumstances. If the thermal shutdown circuits operate against the over temperature, clear the heat generation status immediately.

Depending on the method of use and usage conditions, such as exceeding absolute maximum ratings can cause the thermal shutdown circuit to not operate properly or IC breakdown before operation.

(2) Heat Radiation Design

In using an IC with large current flow such as power amp, regulator or driver, please design the device so that heat is appropriately radiated, not to exceed the specified junction temperature (Tj) at any time and condition. These ICs generate heat even during normal use. An inadequate IC heat radiation design can lead to decrease in IC life, deterioration of IC characteristics or IC breakdown. In addition, please design the device taking into considerate the effect of IC heat radiation with peripheral components.

(3) Back-EMF

When a motor rotates in the reverse direction, stops or slows down abruptly, a current flow back to the motor's power supply due to the effect of back-EMF. If the current sink capability of the power supply is small, the device's motor power supply and output pins might be exposed to conditions beyond absolute maximum ratings. To avoid this problem, take the effect of back-EMF into consideration in system design.

RESTRICTIONS ON PRODUCT USE

- Toshiba Corporation, and its subsidiaries and affiliates (collectively "TOSHIBA"), reserve the right to make changes to the information in this document, and related hardware, software and systems (collectively "Product") without notice.
- This document and any information herein may not be reproduced without prior written permission from TOSHIBA. Even with TOSHIBA's written permission, reproduction is permissible only if reproduction is without alteration/omission.
- Though TOSHIBA works continually to improve Product's quality and reliability, Product can malfunction or fail. Customers are responsible for complying with safety standards and for providing adequate designs and safeguards for their hardware, software and systems which minimize risk and avoid situations in which a malfunction or failure of Product could cause loss of human life, bodily injury or damage to property, including data loss or corruption. Before customers use the Product, create designs including the Product, or incorporate the Product into their own applications, customers must also refer to and comply with (a) the latest versions of all relevant TOSHIBA information, including without limitation, this document, the specifications, the data sheets and application notes for Product and the precautions and conditions set forth in the "TOSHIBA Semiconductor Reliability Handbook" and (b) the instructions for the application with which the Product will be used with or for. Customers are solely responsible for all aspects of their own product design or applications, including but not limited to (a) determining the appropriateness of the use of this Product in such design or applications; (b) evaluating and determining the applicability of any information contained in this document, or in charts, diagrams, programs, algorithms, sample application circuits, or any other referenced documents; and (c) validating all operating parameters for such designs and applications. **TOSHIBA ASSUMES NO LIABILITY FOR CUSTOMERS' PRODUCT DESIGN OR APPLICATIONS.**
- **PRODUCT IS NEITHER INTENDED NOR WARRANTED FOR USE IN EQUIPMENTS OR SYSTEMS THAT REQUIRE EXTRAORDINARILY HIGH LEVELS OF QUALITY AND/OR RELIABILITY, AND/OR A MALFUNCTION OR FAILURE OF WHICH MAY CAUSE LOSS OF HUMAN LIFE, BODILY INJURY, SERIOUS PROPERTY DAMAGE AND/OR SERIOUS PUBLIC IMPACT ("UNINTENDED USE"). ** Except for specific applications as expressly stated in this document, Unintended Use includes, without limitation, equipment used in nuclear facilities, equipment used in the aerospace industry, medical equipment, equipment used for automobiles, trains, ships and other transportation, traffic signaling equipment, equipment used to control combustions or explosions, safety devices, elevators and escalators, devices related to electric power, and equipment used in finance-related fields. **IF YOU USE PRODUCT FOR UNINTENDED USE, TOSHIBA ASSUMES NO LIABILITY FOR PRODUCT.** For details, please contact your TOSHIBA sales representative.
- Do not disassemble, analyze, reverse-engineer, alter, modify, translate or copy Product, whether in whole or in part.
- Product shall not be used for or incorporated into any products or systems whose manufacture, use, or sale is prohibited under any applicable laws or regulations.
- The information contained herein is presented only as guidance for Product use. No responsibility is assumed by TOSHIBA for any infringement of patents or any other intellectual property rights of third parties that may result from the use of Product. No license to any intellectual property right is granted by this document, whether express or implied, by estoppel or otherwise.
- **ABSENT A WRITTEN SIGNED AGREEMENT, EXCEPT AS PROVIDED IN THE RELEVANT TERMS AND CONDITIONS OF SALE FOR PRODUCT, AND TO THE MAXIMUM EXTENT ALLOWABLE BY LAW, TOSHIBA (1) ASSUMES NO LIABILITY WHATSOEVER, INCLUDING WITHOUT LIMITATION, INDIRECT, CONSEQUENTIAL, SPECIAL, OR INCIDENTAL DAMAGES OR LOSS, INCLUDING WITHOUT LIMITATION, LOSS OF PROFITS, LOSS OF OPPORTUNITIES, BUSINESS INTERRUPTION AND LOSS OF DATA, AND (2) DISCLAIMS ANY AND ALL EXPRESS OR IMPLIED WARRANTIES AND CONDITIONS RELATED TO SALE, USE OF PRODUCT, OR INFORMATION, INCLUDING WARRANTIES OR CONDITIONS OF MERCHANTABILITY, FITNESS FOR A PARTICULAR PURPOSE, ACCURACY OF INFORMATION, OR NONINFRINGEMENT.**
- Do not use or otherwise make available Product or related software or technology for any military purposes, including without limitation, for the design, development, use, stockpiling or manufacturing of nuclear, chemical, or biological weapons or missile technology products (mass destruction weapons). Product and related software and technology may be controlled under the applicable export laws and regulations including, without limitation, the Japanese Foreign Exchange and Foreign Trade Law and the U.S. Export Administration Regulations. Export and re-export of Product or related software or technology are strictly prohibited except in compliance with all applicable export laws and regulations.
- Please contact your TOSHIBA sales representative for details as to environmental matters such as the RoHS compatibility of Product. Please use Product in compliance with all applicable laws and regulations that regulate the inclusion or use of controlled substances, including without limitation, the EU RoHS Directive. **TOSHIBA ASSUMES NO LIABILITY FOR DAMAGES OR LOSSES OCCURRING AS A RESULT OF NONCOMPLIANCE WITH APPLICABLE LAWS AND REGULATIONS.**